CENTRO DE INVESTIGACIONES EN OPTICA, A.C.

"COMBINED OPTICAL SETUPS FOR SIMULTANEOUS INSPECTION OF BIOLOGICAL AND ENGINEERING MATERIALS"

"Definitive version. Includes changes suggested by reviewers."

To obtain the Doctor of Science (Optics) degree

Present: M. OM. Gloria del Rosario Frausto Rea

Advisor: Dr. Manuel H. De la Torre Ibarra

Aguascalientes · Aguascalientes · México
November 2020

Dedicatory

To my mother and father, thanks for all your advice and patience.

_____

Acknowledgments

Firstly, I would like to thank God for let me finish in a positive balance this stage of my life and conclude my doctoral studies. I also appreciate my parents' support, which has been an essential part of every task I have accomplished, giving me their trust and being there, both the bad and the good ones. Thanks to their education and teachings, I have been able to achieve all my goals and objectives. I want you to know that I have appreciated all your efforts.

I want to express my gratitude to my thesis advisor Dr. Manuel H. De la Torre Ibarra, who guides me during all these years. I appreciate his time, availability, and patience to answer any doubts during this work and to share all his knowledge and experience in the optics field.

To all my teachers, for giving me their time and sharing their knowledge and experiences. Special recognition to my classmates for their friendship and discussions helped me have an enjoyable time at the CIO.

I want to thank the evaluation committee formed by Dr. Fernando Mendoza Santoyo, Dr. Mauricio Flores Moreno, and Dr. Noé Alcalá Ochoa, who took their time every four months to review the progress of the thesis project.

I also thank Dr. Claudio Frausto Reyes and Dr. Araceli Sánchez Álvarez for reviewing this work. I appreciate your comments and time given to review and evaluate this thesis.

To all the people involved in the project, the mechanical workshop people, the facility cleaner support staff, administrative personal, because each one was an essential part of the work to be carried out satisfactorily.

_____

Figure List

Table List

Content

Abstract

This work introduces two different optical configurations developed to inspect in a non-invasively form biological and engineering samples. The first configuration is an interferometer with a minimum of optical hardware to measure in transmission mode. It is denominated as a transmission digital holographic interferometer (t-DHI). It is applied to retrieve the optical phase from micrometric size semi-transparent biological samples. Our proposed t-DHI system avoids the drawback of this small field of view (FOV) and problematic hardware use when compared with digital holographic microscopy (DHM). The t-DHI setup is used to inspect pollen grains as proof of principle to found a correlation between their size and the phase information. The dimensions of each pollen grain are validated by processing their fluorescence image obtained with the aid of a confocal microscope.

The second configuration introduced is a dual optical set up that simultaneously uses a digital holographic interferometer (DHI) and a Fourier domain optical coherence tomography (FD-OCT). These two independent modules inspect the external and internal optical phase information of composite materials when they undergo a compression load during a mechanical test. The sample under study is a composite material of poly-methyl-methacrylate (PMMA) reinforced with metallic microparticles of copper (Cu). Two sets of specimens with different dimensions are analyzed to compare their mechanical behavior when a home-made testing machine applies a controlled compression load force when both modules are continuously recording. Therefore, the surface and internal optical phases are correlated to the same compression value to have a full 3D displacement measurement.

_____

1. Introduction

Some microscopy techniques, such as classical optical microscopy, can reconstruct high-quality images. This technique has evolved in several already reported configurations such as confocal, phase contrast, near field scanning, bright and dark-field and polarization. Nevertheless, only a few of them use interferometry to retrieve the optical phase and not just the amplitude. Frequently, in the inspection of transparent or semi-transparent micrometric size samples, the digital holographic microscopy (DHM) is employed. This technique gets the phase information about the object under study. However, its drawback is the small field of view and the speckle noise present in the resulting images. Thus, a transmission digital holographic interferometer (t-DHI) is developed in this work, which avoids the drawback of the small field of view current in classical optical microscopy.

This proposed optical configuration measures the size of microscopic pollen grains of the Lantana flower. The optical system can easily manipulate the magnification of the semi-transparent sample projected over a neutral phase screen (NPS). A collimated beam illuminates the microscopic object to prevent geometrical distortion. It is worth to mention that measurements obtained with this proposed optical configuration were validated using a standard and certified step height pattern.

In the mechanical characterization of materials, there are well-defined tests (some invasive), such as magnetic resonance, acoustic emission, ultrasound, and optical techniques. In the last group, digital holographic interferometry (DHI) is used to inspect some samples' surface behavior when they are under a deformation during a mechanical test. This response expresses the total displacement suffered from the specimen, and it has been used to create mechanical descriptions. A similar situation happens with Fourier domain Optical coherence tomography (FD-OCT), but in this case, it gets the internal information of materials under deformation. However, it has not yet been reported an optical setup able to simultaneously get the external and internal data of a sample when tested during a mechanical test.

An optical arrangement is introduced to inspect the internal and external mechanical response of a specimen simultaneously. The system uses two different optical techniques, such as FD-OCT and DHI (referred to as modules). The sample under study is a composite of Poly-methyl-methacrylate (PMMA) reinforced with metallic microparticles of copper (Cu). As proof of principle, two different sets of samples were analyzed to compare their mechanical response. The deformation is for a compression load by a specific testing machine controlled simultaneously as the modules' recording. In this form, each recorded image and measurement is correlated with a particular compression value. The advantage of this proposed set up is the possibility to have complementary information using both sets of measurements to help identify a complex mechanical response.

_____

Thanks to this full analysis of the mechanical behavior of the material under study, it opens the possibility to apply the set up in the biomedical field to analyze biological or hybrid samples.

2. Concepts

2.1 Surface analysis

The present section will briefly describe the basic theory of the main concepts on which this work is based.

2.1.1 Optical Interference

The interference phenomenon occurs when two or more coherent light waves are superposed in space and time. The resulting wave (addition) is a new one with a different or equal amplitude depending on the relative phase for each wave [1]. Figure 1 shows two independent waves (red lines) and their interference wave (black line). In Fig. 1(a), the red waves are in phase, while in Fig. 1(b), they have a phase shift (phase shift of π).

(a)   (b)
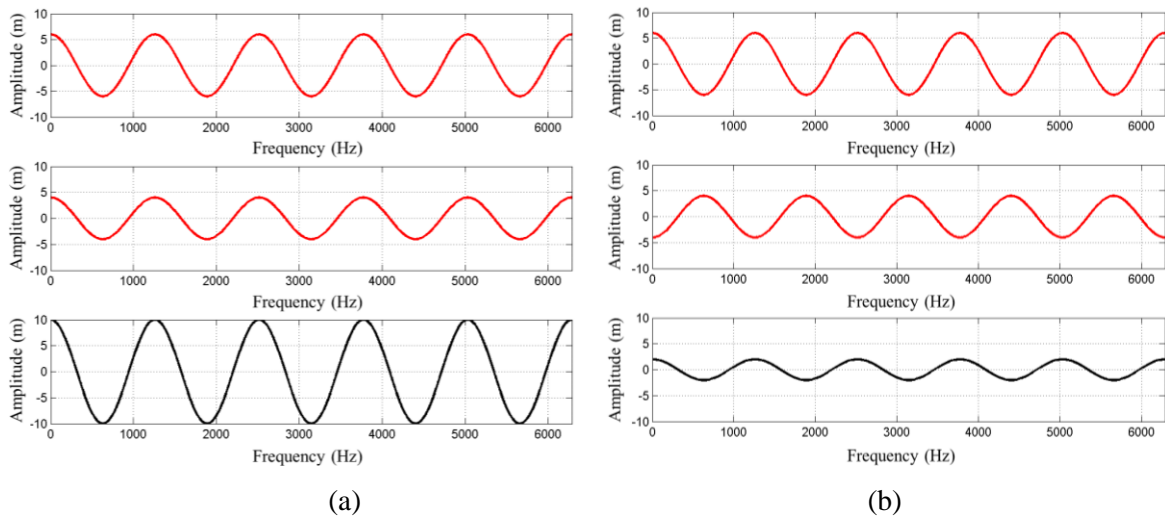
Figure 1. Interference example of two independent waves: (a) in-phase and (b) with a phase shift.

Considering these two waves as:

$$u_1(x,t) = A_1 e^{i\emptyset_1}, \tag{1}$$

$$u_2(x,t) = A_2 e^{i\emptyset_2}, \tag{2}$$

where x is the direction, t is the time, A is the amplitude, and $\emptyset$ is the phase for each one. The resulting wave (interference) becomes:

$$u = u_1 + u_2, \tag{3}$$

$$u = A_1 e^{i\emptyset_1} + A_2 e^{i\emptyset_2}. \tag{4}$$

It is essential to mention that only the intensity is the observable quantity for an optical sensor, and it is the magnitude squared of the electromagnetic field:

$$I = |u|^2, \tag{5}$$

$$I = |u_1 + u_2|^2. \tag{6}$$

Substituting Eq. (1) and Eq. (2) in Equation (6), it results

$$I = A_1^2 + A_2^2 + 2A_1 A_2 \cos(\emptyset_1 - \emptyset_2), \tag{7}$$

reducing and substituting in equation 7,

$$I = I_1 + I_2 + 2\sqrt{I_1 I_2} \cos \Delta\emptyset, \tag{8}$$

where $2\sqrt{I_1 I_2} \cos \Delta\emptyset$ is called the interference term and $\Delta\emptyset$ is the phase difference,

$$\Delta\emptyset = \emptyset_1 - \emptyset_2. \tag{9}$$

The constructive interference is produced when the waves are in phase (cos $\Delta\emptyset$ = 1), and the intensity reaches its maxima; meanwhile, the destructive interference is obtained when the waves are out of phase (cos $\Delta\emptyset$ = -1), and the intensity reaches its minima as Eqs. (10) and (11) show.

$$\Delta\emptyset = 2n\pi, \qquad for \quad n = 0, 1, 2, 3 \dots \tag{10}$$

$$\Delta\emptyset = (2n + 1)\pi, \qquad for \quad n = 0, 1, 2, 3 \dots \tag{11}$$

In Fig. 2(a), it is observed a 1D interference pattern showing a maximum (white) and minimum (black) intensity while Fig. 2(b) shows its corresponding 2D optical interference pattern.
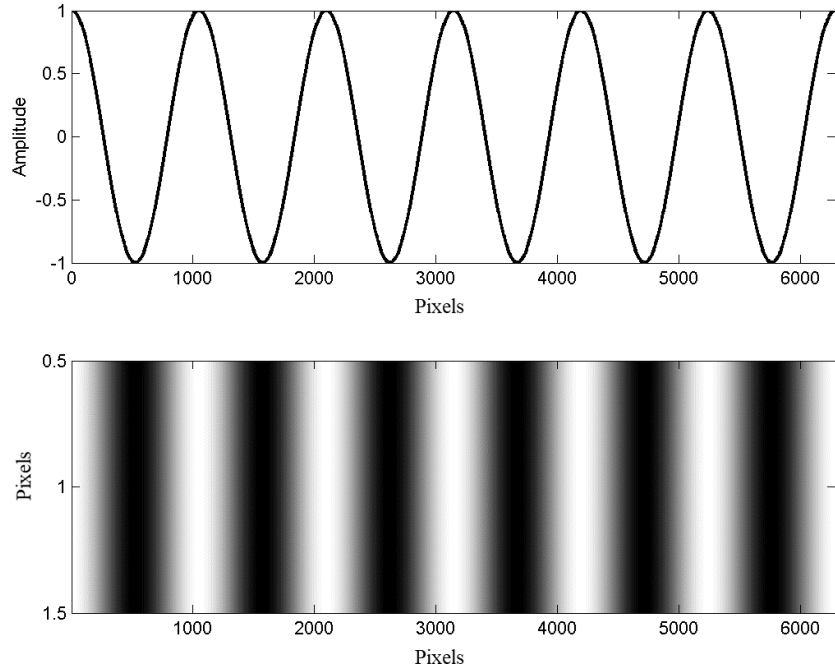
Figure 2. Cosine interference (a) profile and (b) its corresponding 2D pattern.

Now, supposing that $I_1 = I_2$ in Eq. (8)

$$I = 2I_1 + 2I_1 \cos \Delta\emptyset = 2I_1(1 + \cos \Delta\emptyset). \tag{12}$$

Using a trigonometric identity $(2\cos^2(x) = 1 + \cos(2x))$, the Eq. (12) can be rewritten as:

$$I = 4I_1 \cos^2\left(\frac{\Delta\emptyset}{2}\right). \tag{13}$$

There are wavefront and amplitude division interferometers that produce light wave interference. The Young's experiment corresponds to a wavefront division, while Michelson's interferometer is an example of an amplitude division. Fig. 3 is shown a schematic view of Young's experiment; a light source illuminates a screen (S_1) with two slits (P_1 and P_2) where two spherical wavefronts emerged. These wavefronts interfered over a second screen S_2.
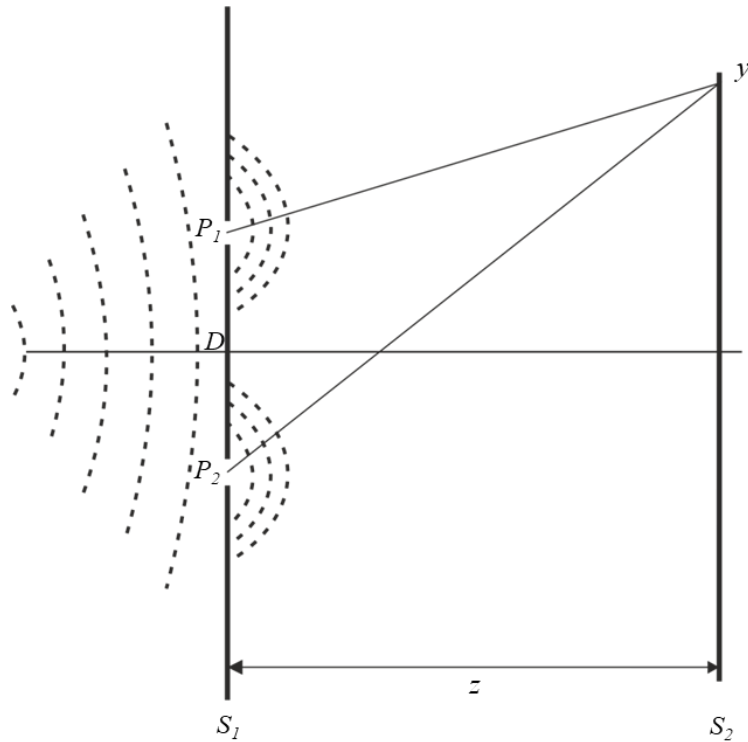
Figure 3. Young's experiment.

By analyzing the geometrical distribution of this setup, it is possible to get a relation of the optical path difference and the phase difference, as Figure 4 shows.

$P_1\left(0, \dfrac{D}{2}\right)$

$P_2\left(0, -\dfrac{D}{2}\right)$
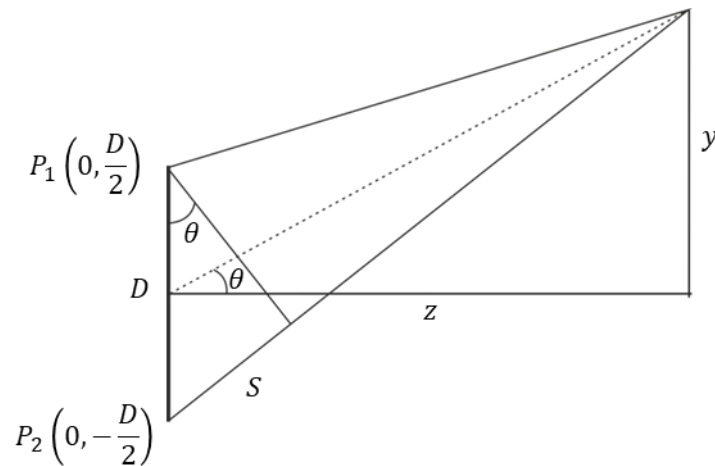
Figure 4. Geometrical Young's interferometer.

Using a paraxial approximation (where $sin\ \theta \approx \theta$) from Fig. 4, it is possible to obtain the following relations:

$$\theta = y/z, \ \theta = S/D, \tag{14}$$

where *S* is the optical path difference,

$$S = yD/z, \tag{15}$$

and the phase difference

$$\Delta\emptyset = kS, \tag{16}$$

$$\Delta\emptyset = kyD/z, \tag{17}$$

where *k* is the wavelength number ($k = 2\pi / \lambda$), replacing the phase difference into the Eq. (13)

$$I = 4I_1 cos^2 \left(\frac{kyD}{2z}\right) = 4I_1 cos^2 \left(\frac{\pi yD}{\lambda z}\right). \tag{18}$$

This expression helps describe the interference pattern at different distances, having a fringe frequency (every 2π) of the wavelength (λ, expressed in meters).

2.1.2 Temporal and spatial coherence

In a monochromatic illumination source, the interference occurs when two or more beams are superposed. However, most of the illumination obtained by a real illumination source is not entirely monochromatic. The phase and amplitude of these illuminations have some irregular fluctuations that decrease the coherence of these illumination sources. When the two beams are coming from the same illumination source, their oscillations (fluctuations) correlate. It is possible to say that those beams could be entirely or partially coherence depending on the coherence term. Nevertheless, two beams coming from different illumination sources will have fluctuations between them, and they are entirely uncorrelated among them. In this case, they are considered as incoherent beams, and interference is not observed. It is essential to mention that, in general, there is not an entirely coherent or incoherent illumination source. The coherence of a particular illumination source could be measured through its temporal and spatial coherence. Both are defined as follows: the spatial coherence designates the correlation between periodic waves signal from one point to another. In

contrast, the temporal coherence implies the phase correlation of waves at a given point in space at two different times.

It is possible to say that light detection is an averaging process in space and time. In equation 8, the average factor is not considered here as the phase difference $\Delta\emptyset$ is assumed to be constant in time. The latter means that u_1 and u_2 have the same single frequency. A light wave with a single frequency must have an infinite length (Fig. 5(a)), a feature not found in current illumination sources. Instead of this, a real source delivers wave trains of finite length (see Fig. 5(b)) with a random phase difference between individual trains.
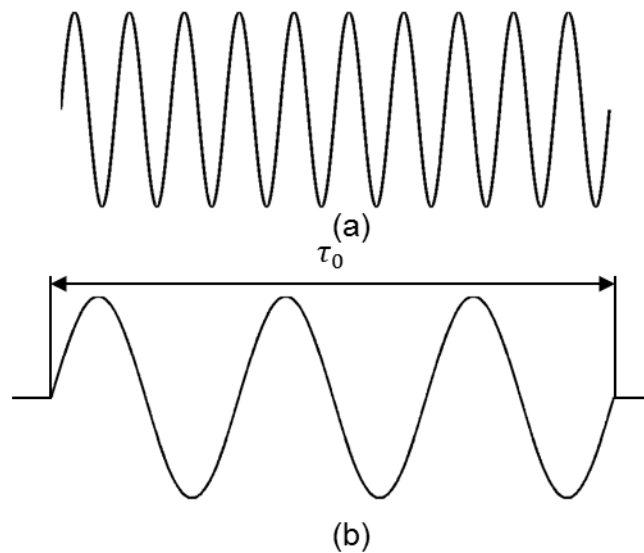
Figure 5. Train pulses (a) infinite and (b) finite.

Michelson's interferometry could be used as an example (Fig. 6) to explain some terms related to coherence.
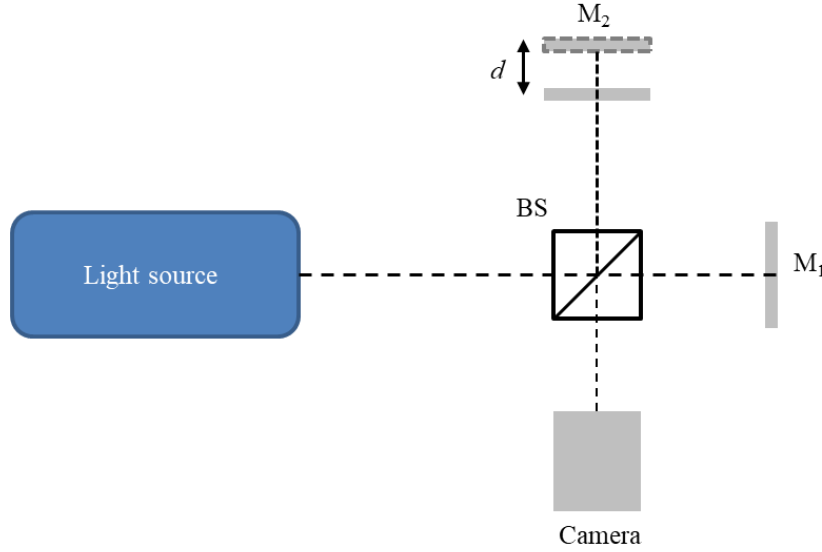
Figure 6. Michelson's interferometer.

In this interferometer, a beam coming from an illumination source is split into two beams (secondary beams) of equal phase; these beams are obtained using a beam splitter BS. Both waves travel in different paths (one to a fixed mirror M_1 and another to a linear translation mirror M_2). These waves are then combined in a camera detector where the interference signal appears.

Considering two waves u_1 and u_2, in a fixed point over the camera sensor, they can be expressed as [17]:

$$u_2(t) = u_1(t + \tau) \ \ or \ \ u_1(t) = u_2(t - \tau), \tag{19}$$

where $\tau = 2d/c$ (the path difference introduces this time delay (τ)), d is a variable distance due to the position of M_2, for this reason, the factor 2 in the value of τ, c is the speed of light. The superposition of a point is:

$$u(t) = u_1(t) + u_2(t), \tag{20}$$

$$u(t) = u_1(t) + u_1(t + \tau). \tag{21}$$

So, the intensity is

$$I = \langle uu^* \rangle = \langle u_1 u_1^* \rangle + \langle u_2 u_2^* \rangle + \langle u_2 u_1^* \rangle + \langle u_1 u_2^* \rangle, \tag{22}$$

where $< >$ denotes temporal average. Assuming that amplitudes are equal in the Michelson interferometer:

$$I = 2I_1 + 2Re(\langle u_1 u_2^* \rangle), \tag{23}$$

the complex self-coherence function $\Gamma(\tau)$ is,

$$\Gamma(\tau) = \langle u_1^* u_1(t + \tau) \rangle = \lim_{T_m \to \infty} \frac{1}{T_m} \int_{-T_m/2}^{T_m/2} u_1^*(t) u_1(t + \tau) \, dt. \tag{24}$$

The integral denotes the intensity of a stationary wave field, and it is the limit of the short time intensity, which is an average of a temporal window centered in t with a width T_m. The equation (24) is the autocorrelation of $u_1(t)$, and the normalized quantity defines the degree of temporal coherence $\gamma(\tau)$:

$$\gamma(\tau) = \frac{\Gamma(\tau)}{\Gamma(0)}. \tag{25}$$

If $\Gamma(0) = I_1$ (this assumption is real) then $|\gamma(\tau)| \leq 1$, and

$$I = 2I_1(1 + Re(\gamma(\tau))). \tag{26}$$

The latter happens in the maximum value of $|\Gamma(\tau)|$. It is essential to mention that both self-coherence and the degree of coherence cannot be measured directly, but the contrast factor V can, as follows:

$$V = \frac{I_{max} - I_{min}}{I_{max} + I_{min}}, \tag{27}$$

$$I_{max} = 2I_1\left(1 + Re(\gamma(\tau))\right), \tag{28}$$

$$I_{min} = 2I_1\left(1 - Re(\gamma(\tau))\right). \tag{29}$$

Substituting Eq. (28) and Eq. (29) in Eq. (27), the contrast factor (also called visibility equation) can be expressed as:

$$V(\tau) = Re(\gamma(\tau)) = |\gamma(\tau)|. \tag{30}$$

The degree of coherence is related to the features of the illumination source, but considering a quasimonochromatic light source whose properties are the sinusoidal variation of the electromagnetic field for a particular time τ_0. Therefore, the phase difference changes abruptly. This time τ_0 is denominated as coherence time. The path difference between the two beams after the beam splitter in the Michelson interferometer should not exceed the measure called coherence length (l_C) and this is expressed as:

$$l_C = c\tau_C. \tag{31}$$

The two wave trains after the beam splitter in the Michelson interferometer have the same amplitude and length, but the resulting phase difference could be different from zero. It is zero when both beams travel the same path length. Although the original illumination fluctuates, the phase difference of the interferometer beams remains constant (Eq. (8)). When the phase difference is different from zero is when one of the two beams travels a longer path length (l) but lower than the coherence length (l_C) ($0 < l < l_C$). However, when the path length is longer than the coherence length ($l > l_C$) there is no interference. The phase difference fluctuates randomly as the illumination successive wave trains are emitted. So, the term $\cos \Delta\emptyset$ varies randomly between -1 and 1 [3]. If many wave trains are averaged, the term $\cos \Delta\emptyset$ will be zero, and the intensity could be expressed as:

$$I = I_1 + I_2. \tag{32}$$

Now, it is possible to express Eq. (8) including the degree of coherence that describes how it is possible to reduce the contrast in the interference pattern:

$$I = I_1 + I_2 + 2\sqrt{I_1 I_2} \, |\gamma(\tau)| \cos \Delta\emptyset. \tag{33}$$

As mentioned before, the spatial coherence describes the correlation in different parts of the same wave. Let's go to use Young's experiment to explain spatial coherence. By considering a punctual illumination source (S_0), which travels to a screen with two slits S_1 and S_2, and whose electromagnetic fields are E_1 and E_2, respectively (see Fig. 7).
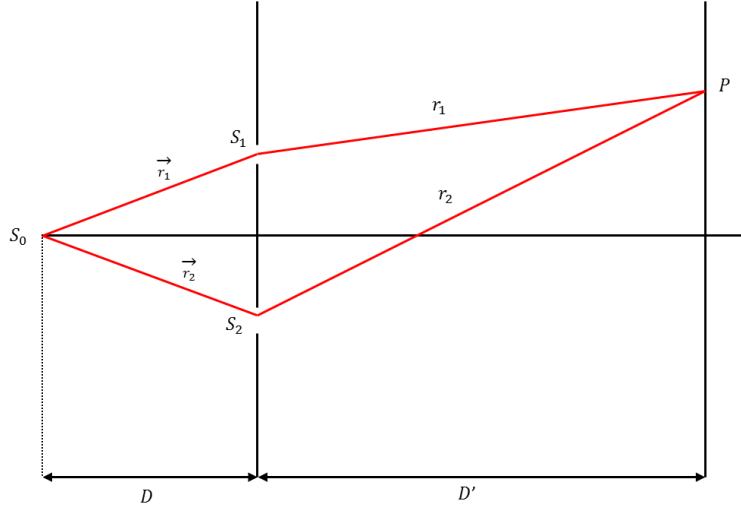
Figure 7. Young's experiment.

$$E_1 = E\left(P, t + \frac{r_1}{c}\right); \qquad E_2 = E\left(P, t + \frac{r_2}{c}\right), \tag{34}$$

where $t_1 = t + r_1/c$ and $t_2 = t + r_2/c$. If $t_2 = t_1 + \tau$, the electromagnetic field can be expressed in Eq.(35). It is possible to define t that is the time that the first secondary light source (from S_1) travels on path one while $t + \tau$ is the time it takes for the second secondary light source (from S_2) to travel the second path.

$$E = E_1(t) + E_2(t + \tau), \tag{35}$$

$$I = \langle EE^* \rangle, \tag{36}$$

$$I = \Gamma_{11}(0) + \Gamma_{22}(0) + 2Re\big(\Gamma_{12}(\tau)\big) = I_1 + I_2 + Re(\Gamma_{12}(\tau)). \tag{37}$$

where $\Gamma_{11}(0)$ is the intensity I_1 at S_1, $\Gamma_{22}(0)$ is the intensity I_2 at S_2, and $\Gamma_{12}(\tau)$ is the Spatio-temporal coherence function. In the experiment, the fringe pattern gives information about the likeness of waves E_1 and E_2 (slits S_1 and S_2) without a time shift. The spatial coherence function ($\Gamma_{12}(\tau)$) helps to express this similarity.

$$\Gamma_{12}(0) = \langle E_1(t) + E_2(t) \rangle. \tag{38}$$

The Eq. (37) can be rewritten as:

$$I = I_0 \left[1 + Re \left(\frac{\Gamma_{12}(\tau)}{\Gamma_{11}(0) + \Gamma_{22}(0)} \right) \right], \qquad (39)$$

$$\gamma_{12}(\tau) = \frac{\Gamma_{12}(\tau)}{\Gamma_{11}(0) + \Gamma_{22}(0)}. \qquad (40)$$

Substituting Eq. (40) in Eq. (39), the intensity is:

$$I = I_0[1 + Re(\gamma_{12}(\tau)), \qquad (41)$$

and the contrast

$$V = Re(\gamma_{12}(\tau)). \qquad (42)$$

2.1.3 Speckle pattern interferometry (SPI)

The speckle phenomenon occurs when a beam illuminates an object's surface, and its roughness produces dark and bright speckles or dots.
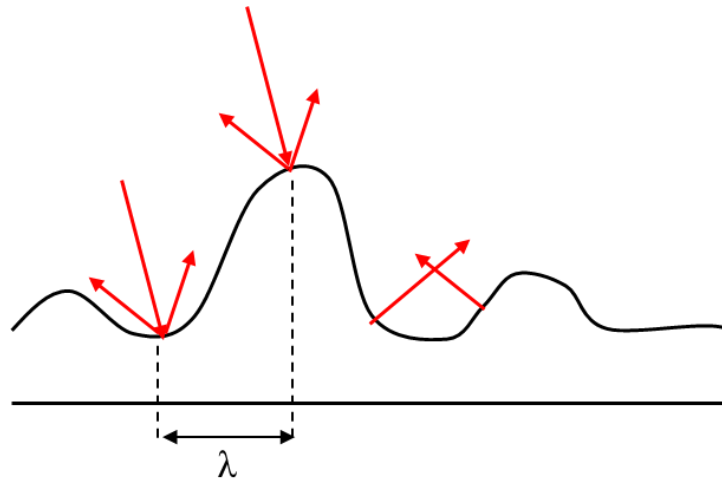
Figure 8. Surface illuminated by a light source that produces speckles.

The speckles result from the light scattered over the surface's points when they are within the range of the illumination wavelength (roughness > λ). The speckle appears when the surface's roughness is

within the size of the illumination wavelength (λ). So, the intensity of the scattered light randomly fluctuates in space, and then dark and bright points appear. There are two types of speckles: subjective and objective. The objective speckle is formed over a screen place at a distance z from the surface illuminated. Here, there is no forming image system between the surface and the screen (see Fig. 9a). The speckle size can be calculated using the spatial frequency equation [3]:

$$f_{max} = \frac{2}{\lambda} sin\left(\frac{\theta_{max}}{2}\right) \approx \frac{L}{\lambda z}, \tag{43}$$

where θ_{max} is the diffraction angle, λ is the wavelength of the light source, and L is the cross-section illuminated by a light source (e.g., laser). Then, the reciprocal of the spatial frequency is the measurement of the speckle's size (ρ).

$$\rho \approx \frac{\lambda z}{L}. \tag{44}$$

On the other hand, the subjective speckle is produced if the illuminated surface is focused on a forming image system (i.e., a lens or the human eye) in a suitable medium such as CCD or a retina for the case of the human eye (Fig. 9b).

(a)   (b)
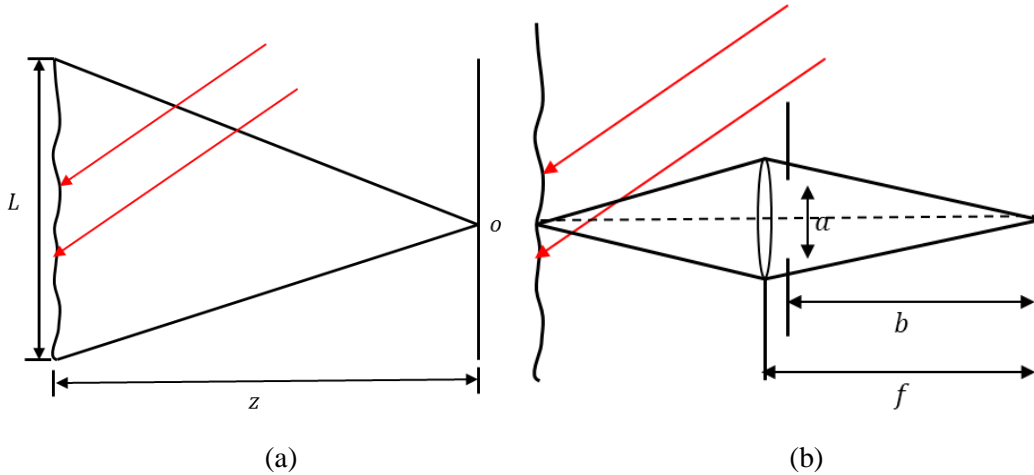
Figure 9. Speckle: (a) objective and (b) subjective where f is the focal length, and a is the lens aperture.

In this case, the spatial frequency and the ρ are expressed as:

$$f_{max} = \frac{2}{\lambda} sin\left(\frac{\theta_{max}}{2}\right) \approx \frac{a}{\lambda f}, \tag{45}$$

$$\rho \approx \frac{\lambda f}{a}. \tag{46}$$

As shown in equation 46, the aperture (a) of the optical system determines the speckle size at the screen or sensor.

The electronic speckle pattern interferometry (ESPI), also called digital speckle pattern interferometry (DSPI), is an optical technique based on the speckle phenomenon that uses laser light to illuminate a particular object whose surface is optically rough. DSPI can detect the displacement or deformation from a sample under study. This optical technique could be set in the out-of-plane (Fig. 10b) or in-plane (Fig. 10a) configuration.

The DSPI in-plane configuration shown in Fig. 10(a) has a laser beam divided by a beam splitter. Both waves illuminate the object, and the backscattering light is collected in the camera sensor. This type of optical arrangement retrieves the sensitivity in one direction, aligned with the resulting plane of the beam directions. Later, in Fig. 10(b), an out-of-plane DSPI, in which a laser beam is divided, generating a reference and object beam is presented. The object beam illuminates the sample, and the backscattering of the object is combined with the reference beam using a beam combiner, and then, both beams are sent to the camera sensor. This configuration has a sensitivity perpendicular to the object's surface due to the illumination direction with respect to the observation direction.

With any type of configuration, it is necessary to match the path lengths of the object and reference beams within the coherence length l_C of the illumination source ($l_C \sim \lambda/\Delta\lambda$, where λ is the center wavelength, and $\Delta\lambda$ is the bandwidth) to observe interference fringes [2]. Besides, in DSPI, as the amplitude is registered directly by the camera, it is necessary to use a phase method to retrieve the optical phase. A common practice is to use the phase stepping method, which requires a piezo driver in one of the beams (reference in the out of plane one) to introduce a controlled phase shift that helps retrieve the relative phase difference. There are techniques with 3, 4, 5, and more phase shifts or phase stepping for these tasks [4]. Another form uses the spatial phase-shifting method where a spatial carrier is introduced to modulate the phase and retrieve the optical phase [5, 6] (all these methods require several images during the process to obtain it). In the following section, an alternative that uses only one image is also described.

(a)

(b)
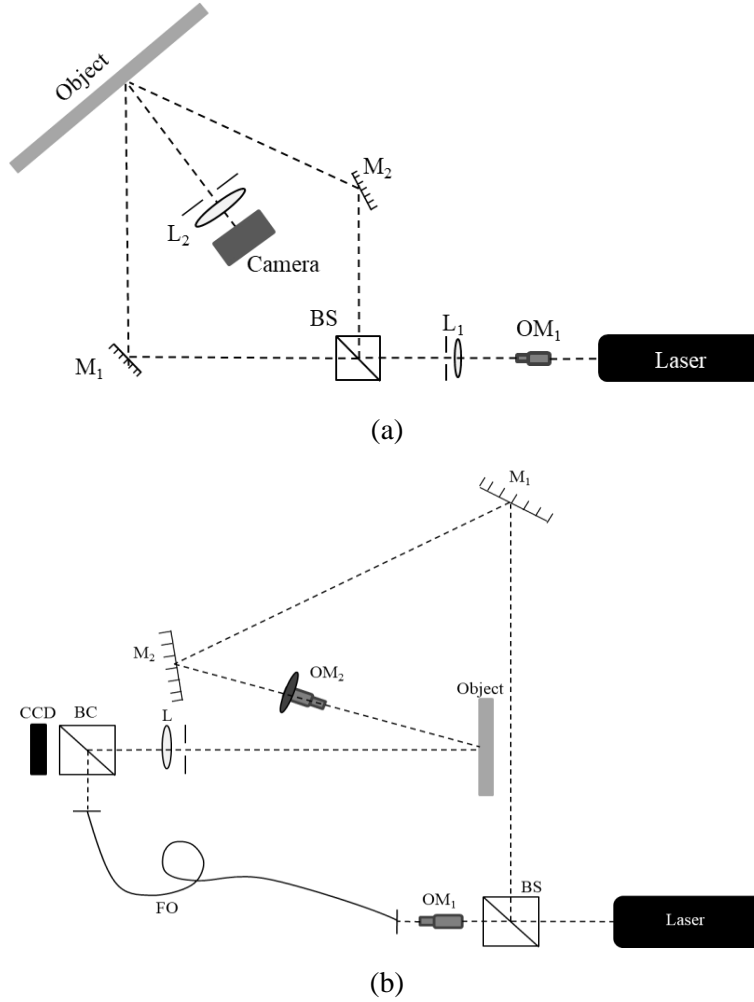
Figure 10. Digital speckle pattern interferometers: (a) In-plane and (b) out-of-plane.

2.1.4 Spatial frequency carrier

It is a method that analyzes a single interferogram image. This spatial carrier technique uses the Fourier transform [7] method to retrieve the optical phase information of a single interferogram. This phase retrieval is widely used in speckle interferometry using digital holographic interferometry (DHI). Here, the camera sensor registers the interference intensity signal $I(x, y)$, expressed as:

$$I(x,y) = a(x,y) + b(x,y)\cos[\Delta\phi(x,y)], \qquad (47)$$

(x, y) denotes the 2D pixel coordinates; meanwhile, $a(x, y)$ and $b(x, y)$ are the background signal and the modulation factor, respectively, while $\Delta\phi$ is the phase difference. Fig. 11(a) is presented as an image hologram. Now, the complex exponential notation is used to rewrite the intensity shown in Eq. (48).

$$I(x, y) = a(x, y) + c(x, y) + c^*(x, y), \tag{48}$$

$$c(x, y) = \frac{1}{2} b(x, y) e^{i\Delta\varphi(x,y)}, \tag{49}$$

where * is used to represent the complex conjugate term, after that, it is necessary to apply the Fourier transform to obtain:

$$FT\{I(x, y)\} = A(u, v) + C(u - f, v) + C^*(u + f, v). \tag{50}$$

Here, the terms (u, v) are the coordinates in the frequency domain, and A is the DC term with the low-frequency variations and the background noise signal. In Fig. 11(b), two side lobes or components are visualized, and the DC term is placed in the central part of the image or spectrum. Only one lobe is necessary to get the information to recover the phase. Thus, a bandpass filter in the spatial frequency domain is applied (removes the complex conjugate term). The bandpass filter is presented in Fig. 12(a), and the component filtered $C(u, v)$ is shown in Figure 12(b). Then, the element filtered is moved to the center, and an inverse Fourier transform is applied to recover the phase information.

(a)   (b)
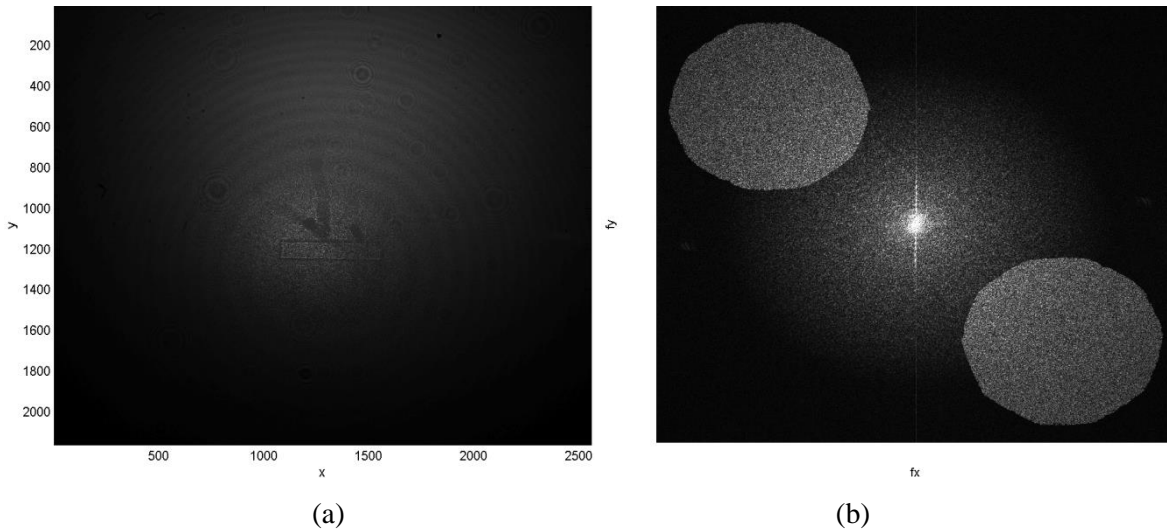
Figure 11. Image hologram (a) Original and (b) its Fourier spectrum.

(a)   (b)
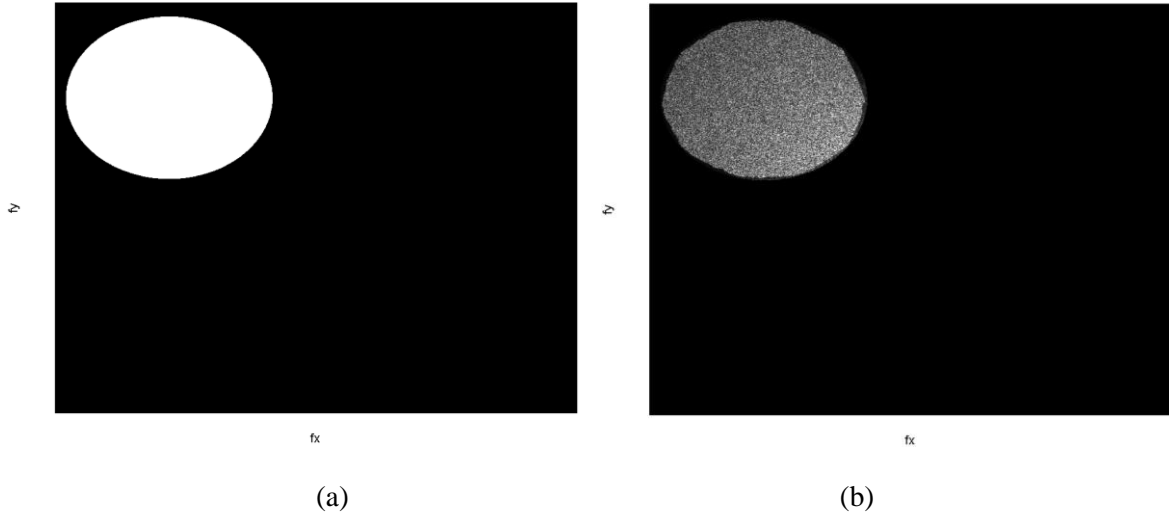
Figure 12. Bandpass filter (a) mask and (b) Spectrum filtered. The *fx* and *fy* terms on the axes represent the u and v frequency, respectively.

2.1.5 Digital holographic interferometry

DHI is an optical technique of two beams and two states that uses a reference beam and an object beam overlapped on an image hologram recorded simultaneously. Two holograms are required to recover the optical phase difference ($\Delta\varphi$), one before, and one after the object undergoes a deformation. In a DHI arrangement, the holograms are registered with a camera's sensor. The whole process mentioned in the previous section is valid in DHI to recover the optical phase information [17]. This phase is expressed as,

$$\Delta\varphi = atan\left[\frac{Re(C_R)Im(C_O)-Im(C_R)Re(C_O)}{Im(C_R)Im(C_O)+Re(C_R)Re(C_O)}\right], \tag{51}$$

where *Re* and *Im* are the real and imaginary parts of the complex values of the inverse transform of the reference (C_R) and deformed (C_O) holograms when both have been filtered, equation (51) obtains the wrapped phase $\Delta\varphi$, which needs to be unwrapped. For this purpose, exists several algorithms dedicated to unwrapping the wrapped phase maps. The result is a smooth optical phase $\Delta\varphi'$ that is used to calculate the displacement map. In particular, for an out of plane configuration, this displacement (*w)* is retrieved using:

$$\Delta\varphi' = \frac{2\pi}{\lambda}(1+cos\theta)w. \tag{52}$$

Here, λ is the wavelength used in the optical system, and θ is the illumination angle between the observation and the illumination directions.

2.1.6 Transmission digital holographic interferometry (t-DHI)

It has been necessary to develop microscopy systems able to inspect the micrometric world. Some of them have been developed to improve their characteristics and allow better results in specific research. In particular, optical microscopy has had rapid growth in its techniques and fundamental principles. It helps to study several biological processes on cells and tissues. High-resolution optical microscopy methodologies are divided as surface methods and three-dimensional methods [8]. Surface methods include techniques such as total internal reflection fluorescence (TIRF), near-field scanning optical microscopy (NSOM), and surface plasmon resonance (SPR). 3D methods are grouped in:

- Reversible saturation.
- Non-linear (multiphoton, second harmonic generation-SHG, two and three-photon, and coherent anti-stokes Raman spectroscopy-CARS).
- Deconvolution method (stimulated emission depletion microscope-STED, harmonic excitation light microscopy-HELM, and others).
- Confocal method
- Interference method (i.e., apotome, structure illumination microscopy-SIM, spatial light interference microscopy-SLIM, image interference microscopy) [9].

These techniques seek to enhance image quality. Within the interferometry group, holography has increased its application in microscopy [10-16]. Examples of the latter are DHI, digital holography (DH), and DHM. All of them have been successfully applied for the characterization of tissues and biological samples.

Perhaps the main advantage of using holography is the content of encrypted information within the hologram. With hologram processing, it is possible to retrieve the amplitude and phase of the deformed wavefront from the sample; propagating the reflected/transmitted sample's wavefront back or forward. The optical phase is used to measure some physical properties such as deformation, stress, strain [17]. Quantitative phase imaging (QPI), which involves several techniques, is now a more active field of a study quantifying cell-induced shifts from the optical path length differences [18]. DHM has been used in the characterization of microscopic biological samples. For example, the dynamic study of live cells [19, 20], the recovery of amplitude images of living neurons in culture

_____

[21]; calculate the refractive index and cellular thickness of mouse cortical neuron cultures [22]; show images of human sperm heads [23]; reconstruct human red blood cells and pancreas tumor cells [24]; and found images of mouse embryo fibroblast cells [25].

DHM creates a non-focused object that appears as being diffracted in the image hologram, an issue that affects the information of an otherwise focused object image [26]. This experimental condition limits DHM applications to only tiny samples that deal with its short working distance and limited field of observation (due to the imaging lens) [27]. It is in this scenario where the t-DHI concept is introduced to have the advantages of DHM with the hardware simplicity of DHI, which will be described in the following lines.

A DHI system, for in-plane or out of plane configuration, operates in reflection mode (Fig. 13 shows an example of the second case), ergo, the sample is illuminated, and a camera sensor collects its backscattering. However, making a change in the object beam could be work in transmission mode to analyze transparent or semi-transparent samples (Fig. 14). So, applying the changes, a transmission digital holographic interferometer is made, which was first used to detect optical phase changes in liquids [28].
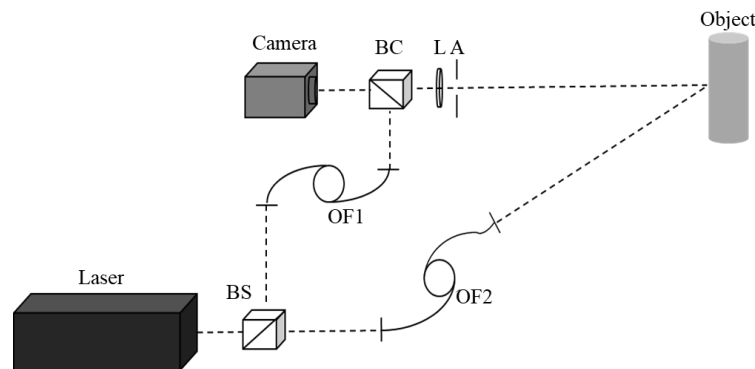
Figure 13. Classical out of plane DHI system.

Analyzing the t-DHI system in Fig. 14, the magnification is achieved with the distance between the optical fiber output (OF2) and the sample. This relation modifies the size projection over the neutral phase screen (NPS).

_____
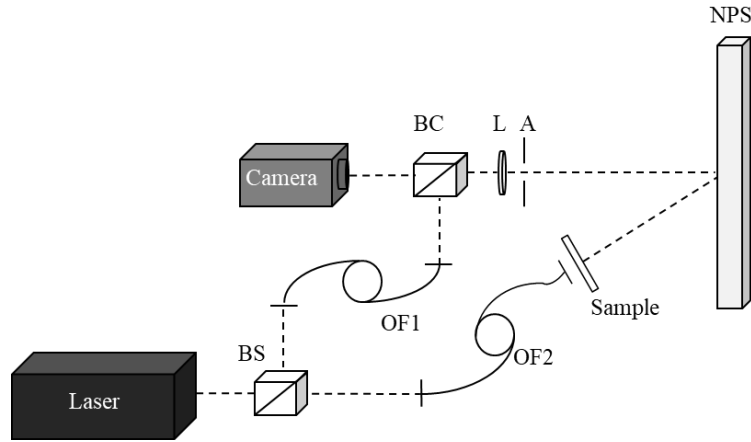
Figure 14. t-DHI system.

However, as this is only a geometrical magnification, there is a limit in it. Then, this optical setup was modified to improve this issue and prevent the introduction of diffraction effects. In the configuration shown in Fig. 15, the object is now illuminated with a collimated beam (using a lens (CL)), and a microscope objective (MO) magnifies this beam on the NPS. As in the previous setup, the backscattering of the NPS is collected by the camera sensor. The controlled magnification is then possible by varying the distance between the microscope objective and the NPS.
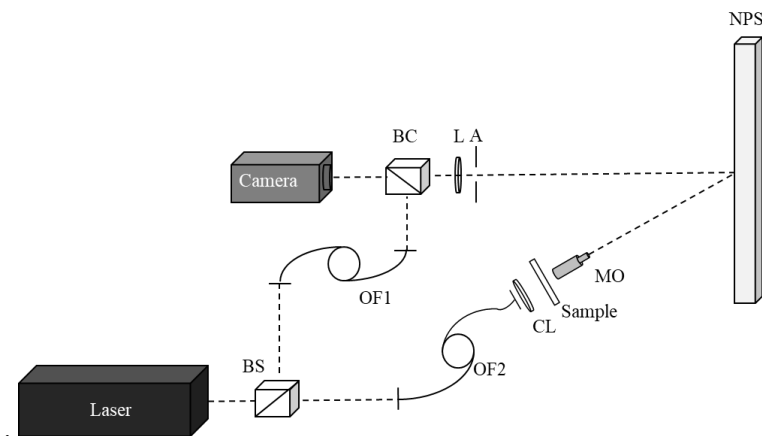
Figure 15. A t-DHI system with variable magnification.

As the t-DHI set up uses as object the projection over the NPS, the retrieved optical phase cannot be directly correlated with the previous relations for phase and displacement (Eq. 52). Thus, it is required to analyze the interaction of the object and the illumination beam that is a plane wavefront. The optical phase is then transformed to be related to a displacement map (w_t) by the next relation,

$$\Delta\varphi' = \frac{2\pi}{\lambda} S_t w_t \,, \tag{53}$$

where S_t is a constant that depends on the sensitivity vector of the experimental conditions, it includes the angle between the observation and the illumination direction.

2.2. Internal analysis

A brief description of the surface inspection was presented, but some optical techniques can inspect the samples' internal information. These optical setups commonly use low coherence length sources, i.e., optical coherence tomography (OCT), based on low coherence interferometry (LCI).

2.2.1 Low coherence length sources

This illumination source has the characteristic of a short coherence length; this could affect the optical path difference (OPD). However, an advantage of these is a generation of less speckle noise. Examples of these sources are laser and super-luminescent diodes (SLD); the last ones operate in the infrared range.

2.2.2 Low coherence interferometry (LCI)

As mentioned before, an interferometer is necessary to match the path lengths of the reference and object beams within the coherence length l_C of the source to observe interference fringes. In contrast to classical interferometry, LCI measures absolute distances. Low coherence interferometry is a non-invasive and non-destructive optical technique based on the existence of fringes if the optical path lengths (OPL) of the sample and reference beams match within the coherence length (l_C):

$$l_c = \frac{2 \ln 2}{\pi} \frac{\bar{\lambda}^2}{\Delta\lambda}, \tag{54}$$

where $\bar{\lambda}$ is the mean wavelength, and $\Delta\lambda$ is the spectral width (Gaussian spectrum assumed). There are two types of LCI: frequency domain and time domain. In both cases, it is used a low coherence light source (such as a super-luminescent diode (SLD) or light-emitting diode (LED)) whose light is directed to a fiber optic coupler which divides the beam in two, one to a reference mirror and other to an object. The combined signal (interference) from both beams is then recorded in a sensor (see Fig. 16).
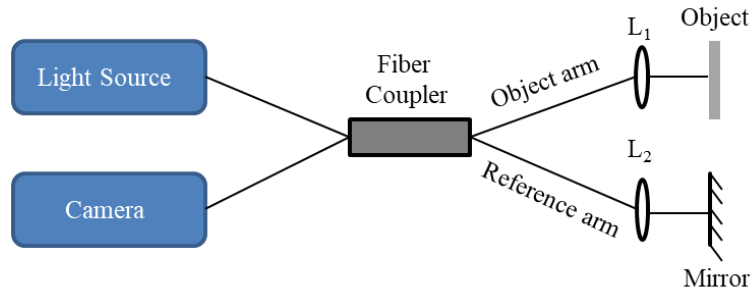
Figure 16. All fiber LCI set up general representation.

2.2.3 Optical coherence tomography

OCT is a non-destructive and non-invasive optical technique based on low coherence interferometry. Mainly, this technique is used to inspect the internal information of scatter material. The result is a cross-sectional image from the internal structure of the sample. Depending on the configuration, OCT can be divided into time-domain optical coherence tomography (TD-OCT), Fourier domain optical coherence tomography (FD-OCT), and quantum OCT. TD-OCT applies the combination of a mechanical scanning mirror in the reference arm and a broadband source.

Meanwhile, the FD-OCT can be divided into swept-source optical coherence tomography (SS-OCT) and spectral-domain optical coherence tomography (SD-OCT). SS-OCT configuration has a fixed reference arm and a scanning light source that send a wavelength once in time (see Fig. 17) while SD-OCT has a fixed arm and a broadband light source with and spectrometer (Fig. 18). In this work, the SD-OCT configuration will be used due to the simplicity of avoiding the scanning devices (scanning mirror) and its synchronizations.
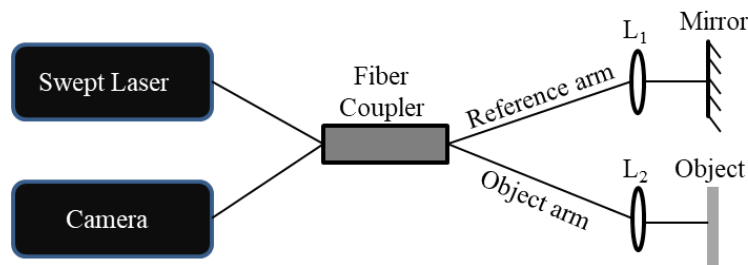
Figure 17. SS-OCT schematic.

2.2.4 Spectral-domain optical coherence tomography

SD-OCT can obtain the tomographic signal of the sample, but also, there is the possibility to retrieve the optical phase information [29]. In this optical system is used a Michelson's interferometer

that counts with an object and reference beam, both beams are directed through a spectrometer (see Fig.18). The spectrometer function is to split all wavelengths. In Eq. (55) is shown the intensity of the interference signal:

$$I(\Delta\lambda, y) = \sum_{\Delta\lambda=\lambda_{min}}^{\lambda_{max}} 2\sqrt{I_R(\Delta\lambda, y)I_O(\Delta\lambda, y)}\cos(\xi(\Delta\lambda, y)), \qquad (55)$$

where I_R and I_O are the intensities of the reference and the object arms, respectively, ξ is the phase or interference term, and λ is the wavelength (within the broadband range min-max).
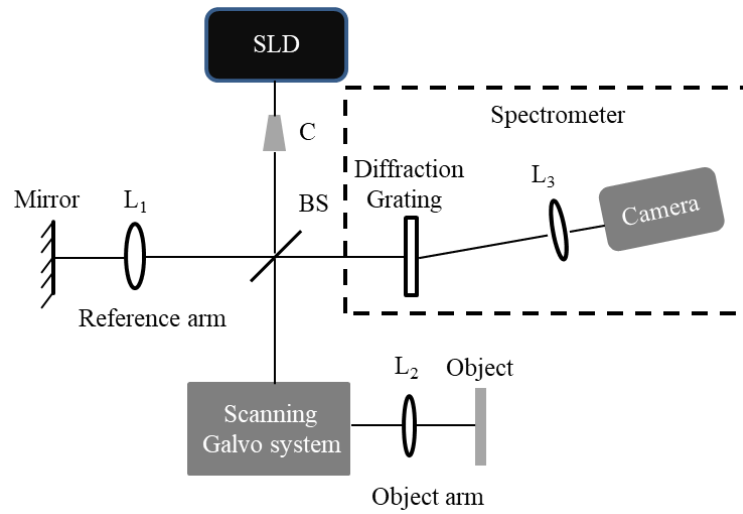
Figure 18. SD-OCT configuration, L_1, L_2, and L_3 are lens; BS is the beam splitter, SLD is the illumination source, and C is the collimation lens.

According to the optical setup's hardware elements, SD-OCT can illuminate the sample under study in a point (also known as A-Scan) or a line (B-Scan) form. When the object beam illuminates as a point over the sample, it requires a galvanometer system to scan several A-scans to construct a B-Scan (2D image). However, if the SD-OCT illuminates the specimen in a line (single-shot mode), it uses a cylindrical lens. Any of these configurations can retrieve the optical phase of the sample due to the help of the spectrometer.

As the line illumination is proposed for this work, the inspection direction is aligned with the y-axis where is the interest region. However, an image before (I_{ref}) and after (I_{mod}) the deformation is necessary as this is a two-stage technique. Both images are needed to retrieve the OCT optical phase map with:

$$\Delta\varphi_{OCT}(z) = atan\left(\frac{Re\{I_{ref}(z)\}Im\{I_{mod}(z)\}-Im\{I_{ref}(z)\}Re\{I_{mod}(z)\}}{Im\{I_{ref}(z)\}Re\{I_{mod}(z)\}+Re\{I_{ref}(z)\}Im\{I_{mod}(z)\}}\right). \tag{56}$$

The wrapped optical phase map $\Delta\varphi_{OCT}(z)$ has values between -π and π represented as black and white gray levels, respectively. Later, an unwrapping algorithm is necessary to get a smooth optical phase. The unwrapped phase map ($\Delta\varphi$') is related to a relative displacement map in the z-axis (w) utilizing the following expression:

$$w = \frac{\lambda_C}{2\pi}(1 + \cos\theta)\Delta\varphi', \tag{57}$$

where λ_C is the central wavelength, and θ is the illumination angle between the observation and the illumination directions for each case.

3. Experimental procedure

In this section, the experimental procedure for two different optical configurations are described; for this reason, they are presented as part 1 and part 2.

3.1 Part 1 (t-DHI with controlled magnification)

In this work, an optical system is introduced based in an out of plane digital holographic interferometer set in transmission mode [28], i.e., the classical optical setup is modified such that micro-sized samples may be inspected without the DHM drawbacks. Besides, the object's illumination and sample are not located in front of the camera, which avoids the sensor's saturation (produced in DHM). So, the object arm is changed to prevent geometrical distortions when the sample under study is magnified. This configuration allows us to have larger magnification ratios reducing the spherical wavefront noise introduced in the microscopic images. The latter avoids the limitations of the working distance and field of view.

The interferometric measurements are validated using a standard precision step displacement specimen with certified dimensions. This validation was also used to prove the cancellation of the spherical wavefront contribution in the optical phase maps. As proof of principle, biological samples whose size is characterized with a commercial confocal microscope are inspected with the proposed transmission DHI system (t-DHI) to relate the phase information with the data obtained from the confocal microscope. The image processing from both systems (confocal microscope and t-DHI) is presented and described before results are obtained, compared, and discussed.

3.1.1 Optical set up

The schematic view of the controlled magnification t-DHI system is presented in Fig. 19, where the illumination source is a Verdi laser at 532 nm with an output power of 200 mW. The laser beam is divided into the reference (RB) and object (OB) beams employing an 80:20 non-polarizing beam splitter (BS), and the reference angle is 15 degrees. Each beam is introduced into a single-mode optical fiber using a spatial filter on a mechanical rig. The object beam coming from the output of the optical fiber is expanded, so a lens (CL) is used to collimate it. After this collimated beam travels through the sample and an infinite corrected microscope objective (μObj) expands it toward a neutral phase screen (NPS), it creates a controlled geometrical magnification. The NPS is sturdy enough to avoid introducing any spurious optical phase variation during the tests [28].
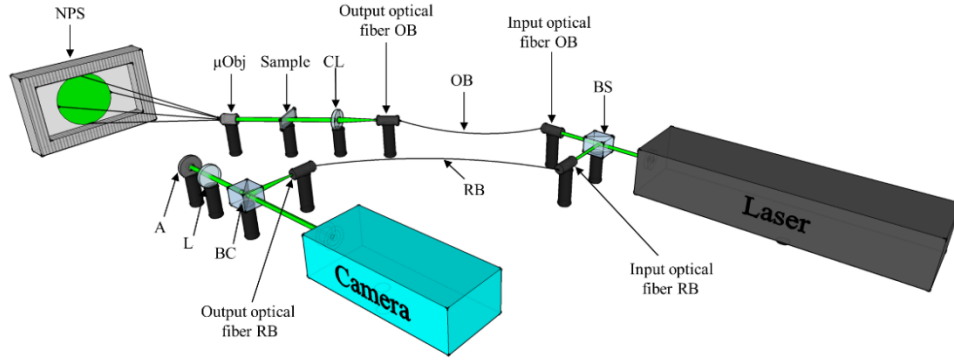
Figure 19. Schematic view of the t-DHI system.

The magnification variation is obtained with the relative distance between the optical fiber output and the sample position, having a size projection over the NPS with the same 20X microscope objective [28], as shown in Fig. 20(a). But, the new configuration in Fig. 19 avoids the introduction of diffraction effects, also removing the spherical distortion. In this new setup, the variable magnification of the object is possible by modifying the distance between the microscope objective and the NPS as it is illuminated with a collimated beam. Fig. 20(b) and Fig. 20(c) are shown a comparison of these two forms of magnification. It is important to note that in Fig. 20(c), a tilting plane profile is more evident than in Fig. 20(b) due to the collimation. The tilting profile is present because the illuminated sample does not have parallel surfaces.

The magnified object's projection over the NPS is focused on the camera sensor by a lens (L) combined with an aperture (A). The light coming from the reference beam is sent to a 50:50 non-polarizing beam combiner (BC), where it directed and further overlapped on the camera sensor with the backscattered light from NPS. This interference pattern is recorded with an sCMOS sensor (PCO EDGE) with 2560 x 2160 pixels working at a dynamic range of 12 bits. The camera is recording an area over the NPS of 160 x 135 mm.
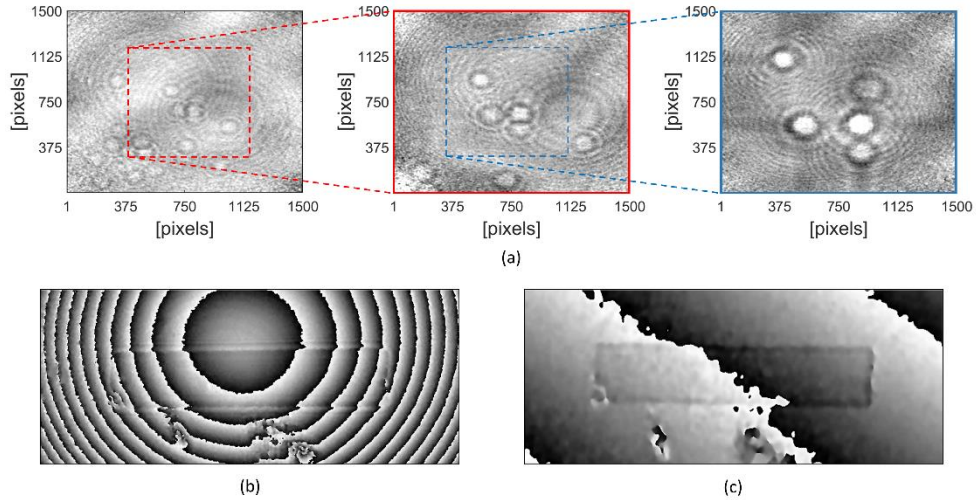
Figure 20. (a) Example of three different FOV using the variable magnification and keeping the same camera's resolution retrieved wrapped phase map for a standard calibration pattern, using either the (b) geometrical [28]; or the (c) controlled magnification (Fig. 19) setups.

3.1.2 Validation

For validation purposes, a precision displacement specimen (model EMD-09000W3) from Federal Products Corporation is used, with a step or height of 5.03 µm and an accuracy of ± 0.127 µm as Fig. 21(a) shows. The standard calibration pattern was placed in the object arm of the t-DHI system shown in Fig. 19, and the optical phase map of the pattern is presented in Fig. 21(b). The optical phase profile for a linear section (red line in Fig. 21(b)) is shown in Fig. 21(c): it is possible to observe the step and the expected speckle-noise added. With these results, it is possible to validate the measurements and the controlled magnification of the proposed optical system.
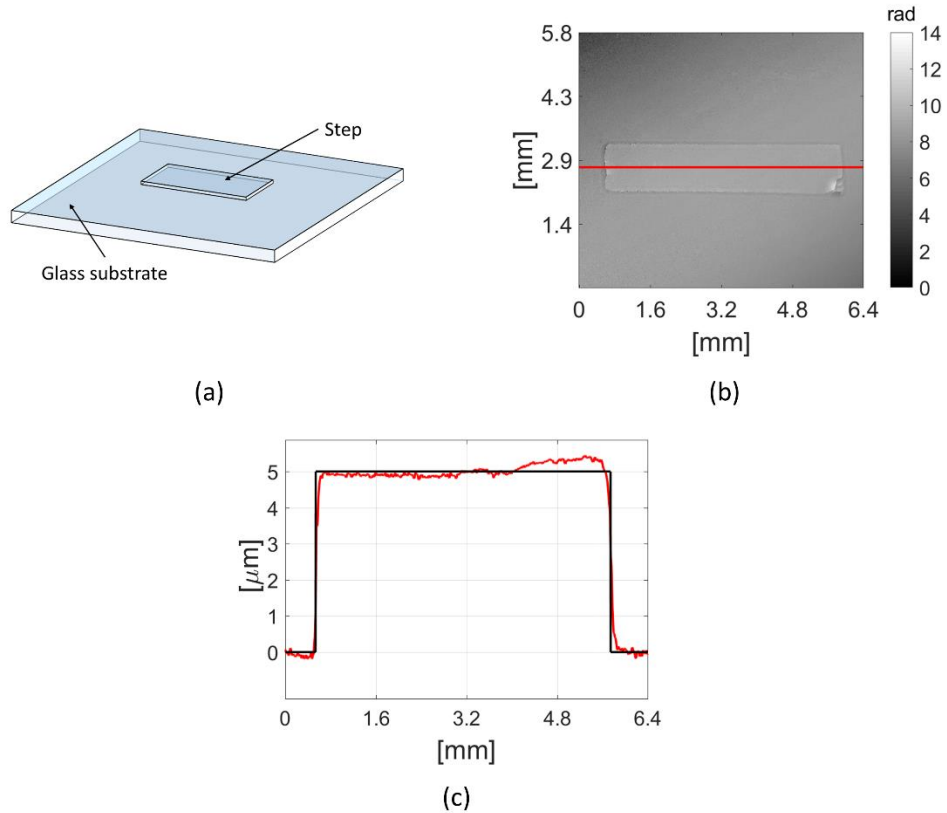
Figure 21. Standard calibration pattern, (a) schematic, (b) unwrap phase map, and (c) profile of the step.

3.1.3 Biological sample

The microbiological samples used are pollen grains from the Lantana flower [30-33], selected due to their simplicity to be characterized in a well-established microscopic technique such as the confocal microscopy. Prepared pollen grain samples are commonly used in multiphoton microscopy and are imaged in confocal microscopy: this is the reason to use them in this t-DHI system for comparison purposes. In appendix A presents both the type of flower used and how the sample under study was prepared. The example utilized in this work is referred to as the pollen fixation arrangement (PFA), see Fig. 22.
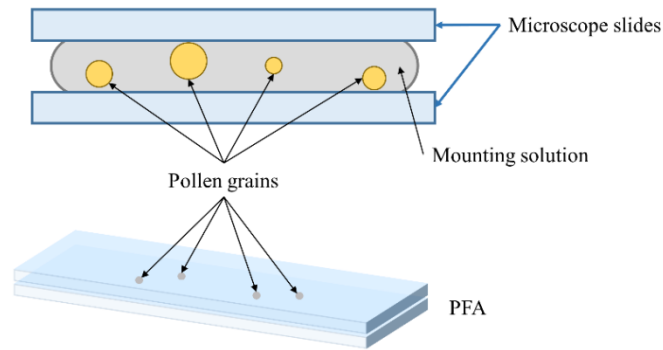
Figure 22. Pollen fixation arrangement.

Several PFAs were made to obtain the information of the specific region of each PFA.

3.2 Part 2 (Simultaneous inspection DHI+OCT)

Engineering materials could be mainly classified into metals, ceramics, polymers, and carbon, but some applications require particular properties that are impossible to achieve individually. When two or more different materials are combined, a composite material is obtained, which has a different mechanical response than its raw materials [34]. Composites materials have a base material called matrix mixed with a reinforcement [35]. These reinforcements could be particles [36, 37] or fibers [38] embedded in the matrix. It is essential to mention that composite materials' use is continuously growing due to the need to have particular features. The aeronautics industry requires light and resistant materials to improve fuel consumption, among other desired features [39,40]. A similar case is found in materials based on cement, which are mixed with carbon nanotubes (CNTs) or carbon nanofibers (CNFs) to improve their properties within the construction industry [41].

There are several well-established tests to characterize a material mechanically. Some tests have a certain degree of invasiveness; however, the introduction of the non-destructive testing simplifies and avoids damage to the object under study. Some examples are magnetic resonance, acoustic emission, ultrasound, optical techniques [42-44]. Especially, the optical non-destructive testing methods allow high-resolution information of the sample in a remote and non-invasive way [45]. For non-destructive internal inspections, the optical coherence tomography (OCT) could be used. It gives cross-sectional images of the material's internal structure, taking advantage of the low–scattering property. This technique was first devoted to inspecting optical fibers [46], but after that, it was quickly applied in ophthalmology [47, 48] to obtain corneal and retina images [49]. Its current application is found in dermatology [50,51], dentistry [52,53], cardiology [54, 55], art [56], materials science [57], mechanical testing [58, 59], among others. It is important to mention that OCT has been used to obtain

the mechanical behavior of materials during tests of tensile strength and fracture [38, 60], crack formation [61], deformation [62], homogeneity [63]. Tomographic images from OCT help to analyze the internal microstructure of the samples under study. According to its configuration to acquire the interference signal, OCT could be divided into Spectral-domain OCT (SOCT), time-domain OCT (TD-OCT), and quantum OCT. For SOCT, when the method to retrieve the spectral signal is the Fourier transform, it is known as Fourier domain OCT (FD-OCT), which has the advantage of registering a tomographic image (B-scan) in a single shot without scanning devices. FD-OCT can retrieve not only the tomographic signal but also the optical phase information [64].

On the other hand, for non-destructive surface inspections is the ESPI (also known as DSPI). DSPI's optical phase information retrieval can be carried out with two different methods: one of them uses a phase-shifting (PS-DSPI). The other uses a spatial carrier, and an image hologram is obtained, and it is referred to as digital holographic interferometry (DHI). DHI's surface information could give the mechanical response of a material: strain, residual stress, displacement, stiffness, and many more [65-68].

As it was mentioned before, each technique could give information regarding the mechanical response of the object. Thus, in this work, DHI and FD-OCT are simultaneously applied to inspect a composite specimen during a controlled mechanical test. In mechanical characterization [69] typically involves several tests such as compressive strength, tensile strength, impact resistance, fracture toughness, fatigue [70, 71]. The compression test indicates the material's response to crushing and its reaction to the applied force. However, during the test, the sample may suffer bending previously to its failure. The bending is prevented using short and thick specimens, and commonly, a testing machine is used to perform this compression in a controlled way. It is possible to have tests of break stress, compressibility and recovery, compressive hardness, compressive deformation, compressive strength, ultimate compressive strength, and others [72, 73].

In this work, the sample under study is a composite material based on a matrix of PMMA reinforced with metallic microparticles of copper (Cu) is tested for compressive deformation. Composite specimens with a rectangular prism shape (see Fig. 23) were compressed through a home-made compression testing machine (CTM). High repeatability and a smooth load application are achieved due to the CTM control system (see Appendix B). The latter is a critical condition required to match with the high resolution of DHI and FD-OCT. Results show a correlation between the internal and the surface deformation response of the material.

The composite material is analyzed in the xy plane (surface inspection) with the DHI system (blue blocks), while a B-scan in the yz plane (internal inspection) is observed with the FD-OCT system (green blocks). Also, a common region seen by both techniques is shown (yellow blocks).
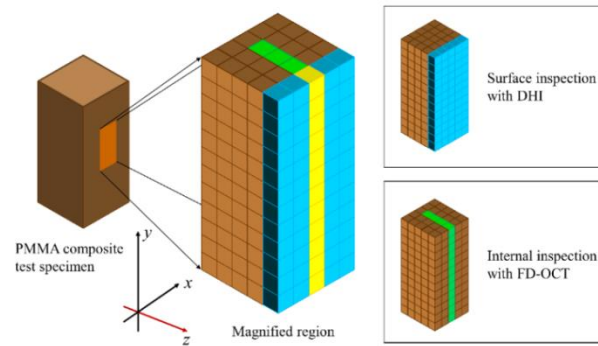
Figure 23. Schematic view of a composite specimen indicating the inspected regions.

As the compression test is inspected with two optical techniques, a dual configuration is used for this optical set up (this implies two different setups sharing a reduced space). In Fig. 24 presents the final layout, consisting of an FD-OCT at the same sample's level and the DHI on top of the OCT system.
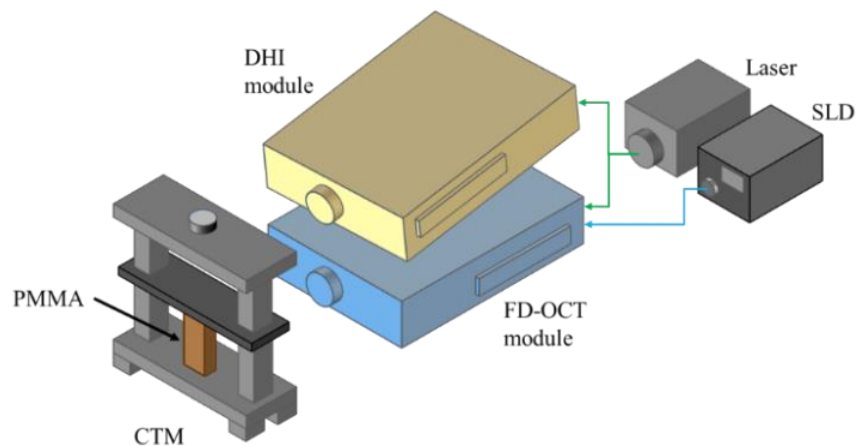
Figure 24. General schematic view of the dual inspection system with the DHI and FD-OCT modules.

The detailed optical diagrams for the DHI and FD-OCT systems are presented in Fig. 25 and Fig. 26, respectively. The DHI module uses a solid-state laser at 532 nm with a variable output power set at 50 mW due to the small specimen's size. This laser beam is divided into the object (of_obj) and the reference (of_ref) arms, which travel through single-mode optical fibers. The reference beam is directed in front of a beam combiner (BC), illuminating the camera's sensor (Camera). The object beam illuminates the composite specimen with an angle of 15°. The sample's backscattering is

collected using a lens (L) and aperture (A), which combines this backscattering with the reference beam at the camera. The CMOS camera has 1280 x 960 pixels at 10 bits, which registers the entire PMMA sample.

Meanwhile, the FD-OCT module is configured to acquire a B-scan in a single shot and uses a super-luminescent diode centered at 840 nm with broadband of 50 nm and 15mW the illumination source. This infrared broadband source is launched with the DHI's laser to a 2×2 optical coupler (OC) for alignment purposes. One coupler output port is blocked while (B) the second one is collimated and divided into the reference and the object arms utilizing a beam splitter (BS2). The reference beam is reflected by a gold-coated mirror and then is redirected to a reflection diffraction grating (G).
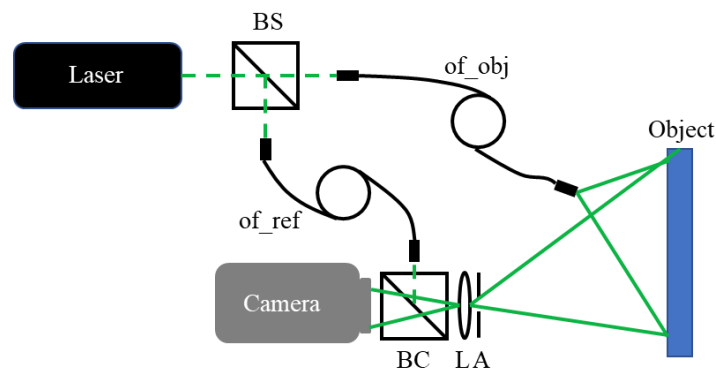
Figure 25. Detailed schematic view of the DHI system, BS is a beam splitter.
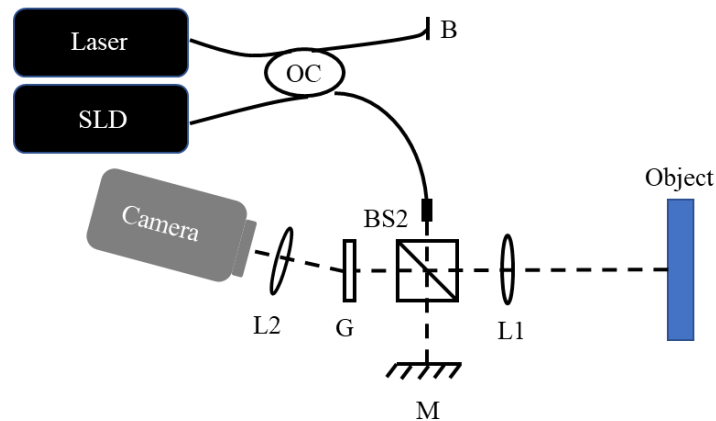
Figure 26. Detailed schematic view of the FD-OCT system.

The composite specimen is illuminated with a lens (L1), and its backscattering is diffracted together with the reference beam to be focused on the second camera's sensor using a lens (L2). The grating

has 1200 l/mm, and the camera's sensor has 1280 x 1024 pixels at 10 bits, which registers the entire SLD signal. Both FD-OCT and DHI systems are aligned precisely to the same object's distance to have well-focused the PMMA sample, as Fig. 27(a) shows. In Fig. 27(b) is presented a composite specimen undergoing a compression force so that this material suffers a plastic deformation.

(a)　　　　　　　　　　(b)
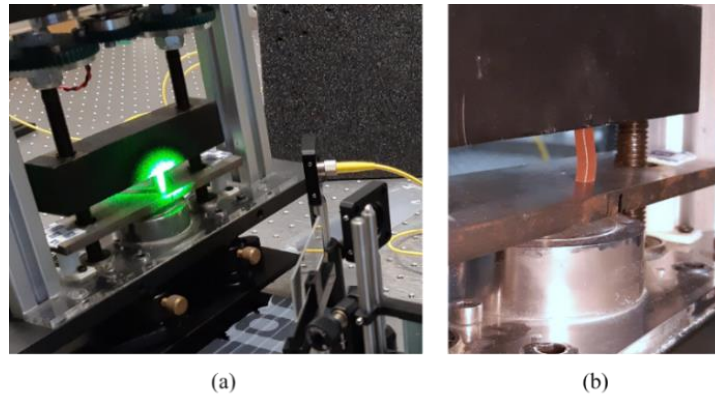
Figure 27. Experimental images showing a specimen (a) illuminated during a compression test and (b) close up showing a plastic deformation.

_____

4. Results

4.1 Part 1 (Transmission digital holographic interferometry)

Each PFA was placed in the object beam's path, and several image holograms were recorded for an extended time. When these holograms were processed, it was confirmed that the motion of the solution introduced any optical phase. Besides, this process also helps as a repeatability test for different PFAs where selected regions are inspected. The PFA's observed areas were labeled to compare the interferometric signal with the information obtained from a Zeiss model LSM 710-NLO confocal/multiphoton microscope.

The confocal microscope measures each pollen size of the selected PFA's regions using a 10X microscope objective in an image with a dimension of 860 x 860 µm (whose total magnification is approximately 100x). This confocal microscope can generate transmission, fluorescence, and compound (sum of the transmission and fluorescence images). Then, the resulting confocal measurements are compared with the optical phase information (t-DHI) using a home-made algorithm that matches the observed regions between both techniques. Four different samples are presented in this section: PFA_a, PFA_b, PFA_c, and PFA_d. Figures 28(a) and 28(b) show the fluorescence confocal microscope image and the t-DHI image (unwrapped phase map), respectively, for the PFA_a sample. The unwrapped phase map is obtained using a minimum- cost-matching algorithm named PV_SPUA2 from Phase Vision.

Figure 28. Images for a PFA_a sample: (a) confocal and (b) t-DHI. Please note that t-DHI has a larger field of view.

In this PFA_a, there are fifteen pollen grains, but in the confocal image, only eight pollen grains are sharply focused; the others are unfocused (red marks). For this reason, in this sample, only the

_____

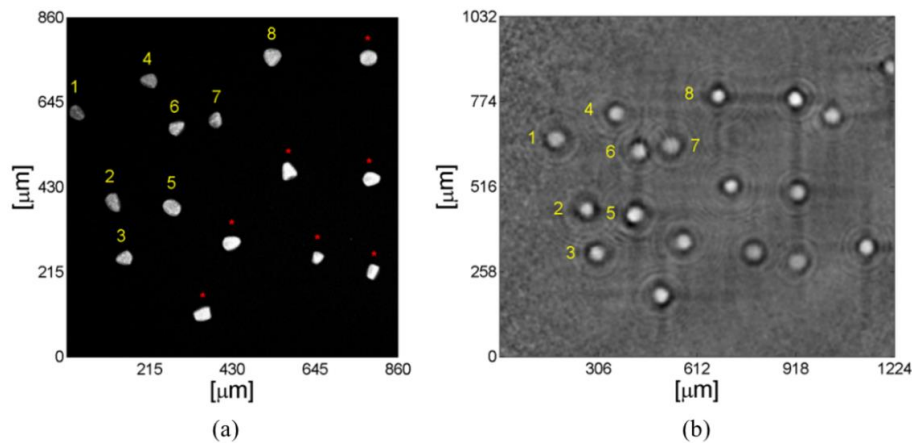numbered pollen grains were analyzed. By means of the unwrapped phase map, it is possible to get the intensity phase value for each pollen grain, while with the confocal image, it is possible to obtain its dimensions. Fig. 28(a) shows that pollen 8 is the largest of all and that pollen grains do not have the same geometry, ergo, some are elliptical, circular, triangular, or some have other irregular forms indeed. Thus, it is necessary to obtain the area of each pollen grain instead of merely its x and y dimensions. The area (confocal microscope) and optical phase intensity (t-DHI) measurements for every pollen grain are calculated and presented as bars in Fig. 29. To process the confocal image, a digital image processing algorithm to obtain the perimeter of every pollen grain was made. The later helps to calculate a pixel area to convert in an area (m^2). Then, the optical phase intensity is retrieved using the unwrapped phase map, and an algorithm averages a neighborhood around each pollen's maximum phase value. In this manner, it is possible to corroborate that the pollen grain 8 has a more considerable intensity value and the greater area. At the same time, the element 7 is the smaller in the area and intensity value.
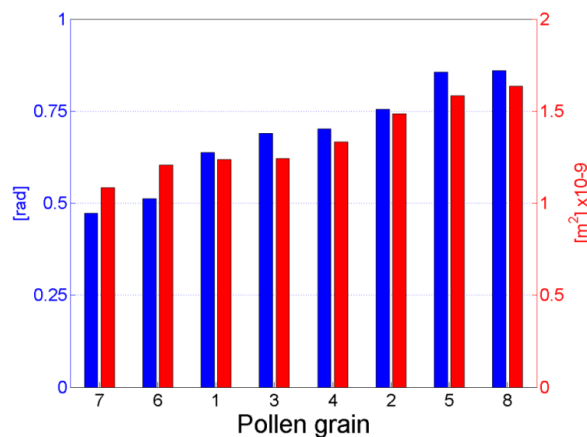
Figure 29. Optical phase intensity and area for every pollen grain of Fig. 28.

Once the hypothesis of size and phase correlation was confirmed, new PFAs are inspected where different sample conditions are analyzed. Next, samples PFA_b, PFA_c, and PFA_d were measured. Fig. 30(a) and Fig. 30(b) are observed the confocal and t-DHI images from the PFA_b sample, respectively. This PFA shows four different cases of samples' distribution, as described in Table 1. The confocal transmission image and the processed optical phase map image are shown in Fig. 31. In this sample, particle 6 has the maximum intensity phase due to the addition of two pollen grains, which one of them has an irregular form, and it produces an overlapping in the phase map of the t-DHI image as Fig. 31(b) shows. This intensity value is considerably increased due to the sum of each pollen grain's intensities, a feature shown in Fig. 31(c).

Table 1. Conditions observed in PFA_b

The situation between two pollen grains	Pollen grains involved
Large separation	1 and 5
Regular separation	3 and 4
Short separation	2 and 3
Nearly overlapped	6*
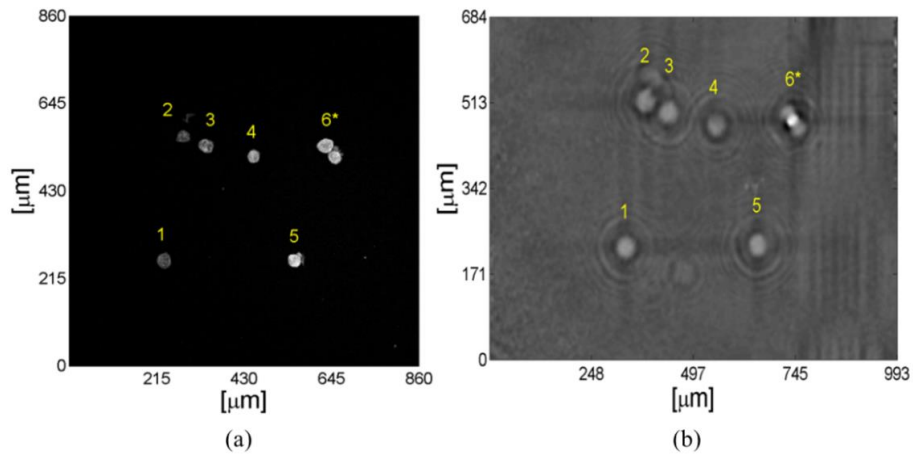
Figure 30. Sample from PFA_b showing an overlapping case (indicated by *): (a) Fluorescence image and (b) unwrapped optical phase map.

From Fig. 31(c), it is possible to observe the two peaks corresponding to each pollen grain of particle 6, with the phase intensity increased over the central part (red arrow). Fig. 32 shows the area and intensity value for each pollen grain of PFA_b. As expected, if the overlapping factor is omitted, particle 6 will appear as the biggest one, and the pollen grain 4 is the smaller, both in area and intensity, showing a direct relationship between both measurements.
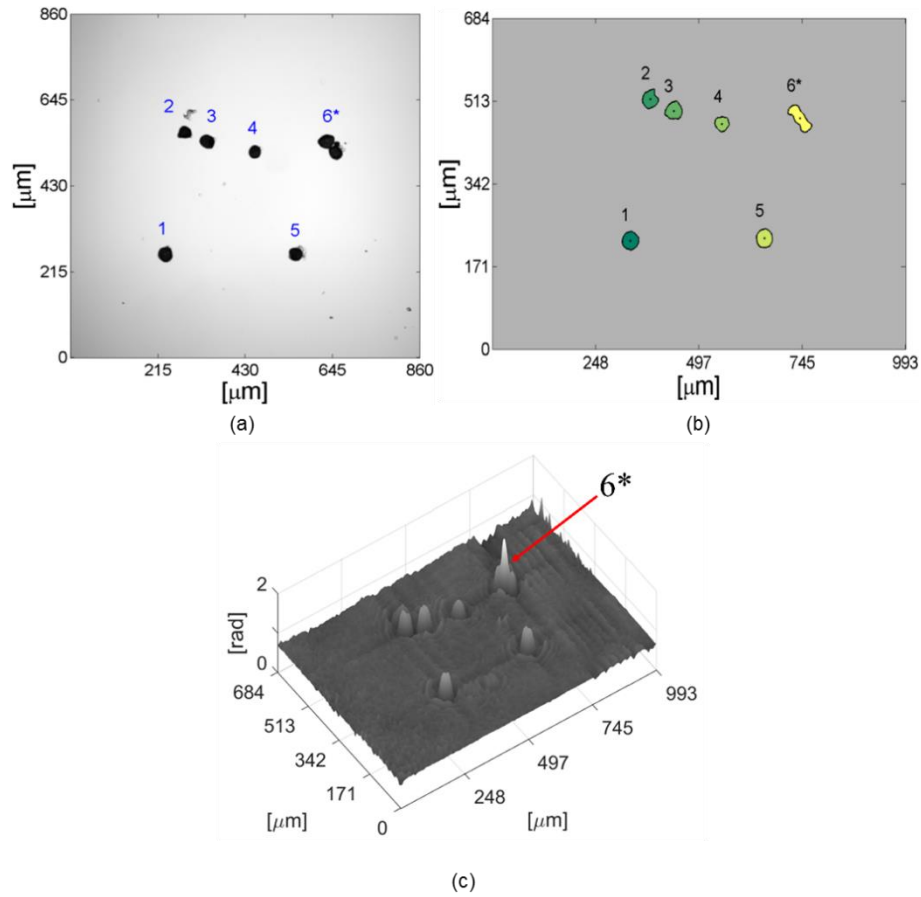
Figure 31. PFA_b sample: (a) confocal transmission image, (b) t-DHI labeled image, and (c) 3D mesh plot obtained from the unwrapped phase map.
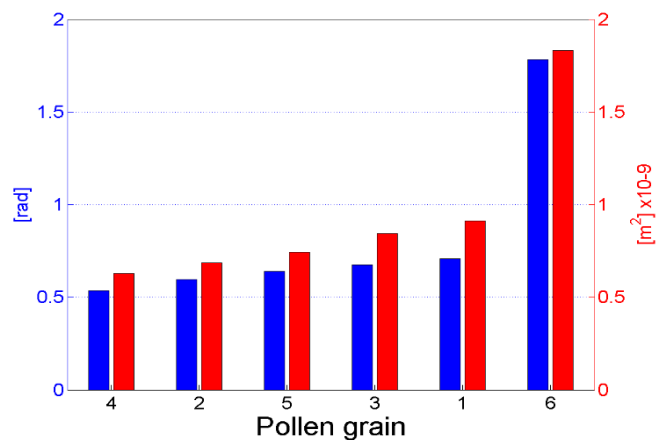
Figure 32. Optical phase intensity and area measurements from PFA_b.

The next sample is the PFA_c; its fluorescence and t-DHI images are presented in Fig. 33. The pollen grains were labeled for both images, with their phase intensity and area shown in Table 2. Following Table 2, Fig. 33(c) shows the 3D view of the optical phase magnitude for each pollen grain in the PFA_c sample.

Table 2. Measurements of the PFA_c sample

Pollen	Phase intensity (rad)	Area [m^2 x10-9]
1	1.794	1.54
2	0.791	1.13
3	0.607	1.03
4	0.256	0.55

(a)

(b)

(c)
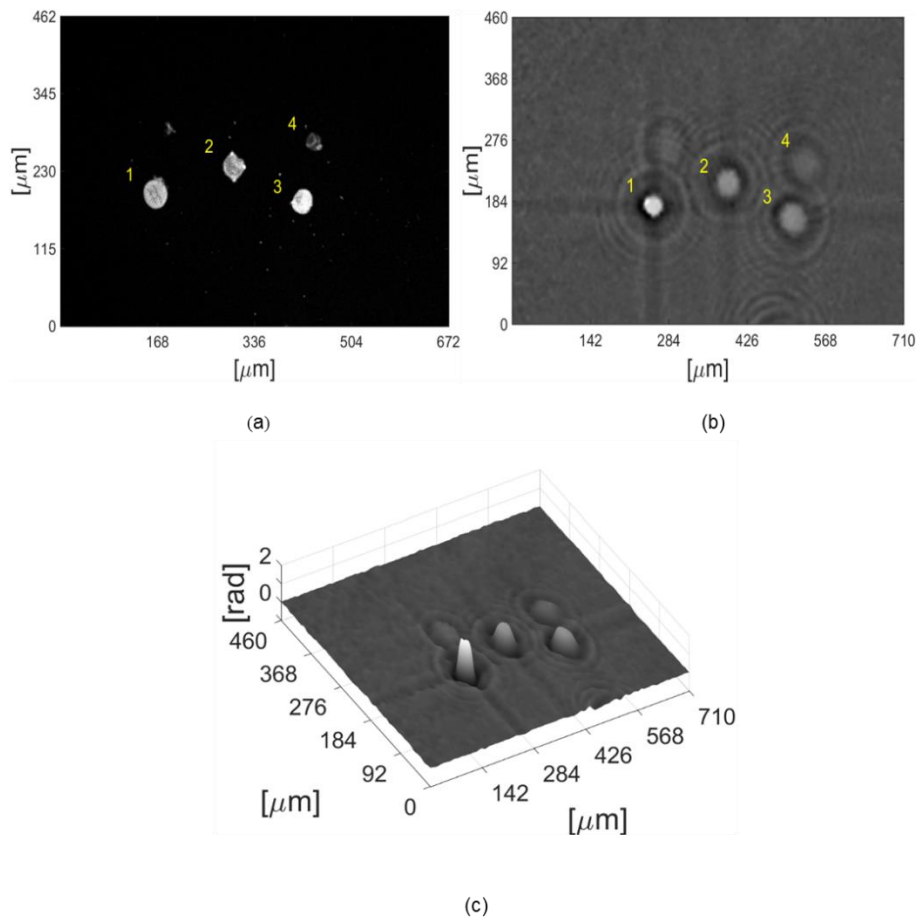
Figure 33. PFA_c sample: (a) fluorescence, (b) 2D unwrapped phase map and (c) 3D unwrapped phase map image.

Finally, PFA_d shows two pollen grains that appear very similar in size when observed with the confocal microscope, as Fig. 34(a) shows. Still, they are successfully differentiated employing the optical phase, as Fig. 34(b) shows.

Table 3. Measurements of PFA_d

Pollen	Phase intensity (rad)	Area [m^2 x10-9]
1	1.599	1.70
2	1.552	1.67

The PFA_d measurements are given in Table 3, where it can be seen that the two pollen grains' area difference is minimum.
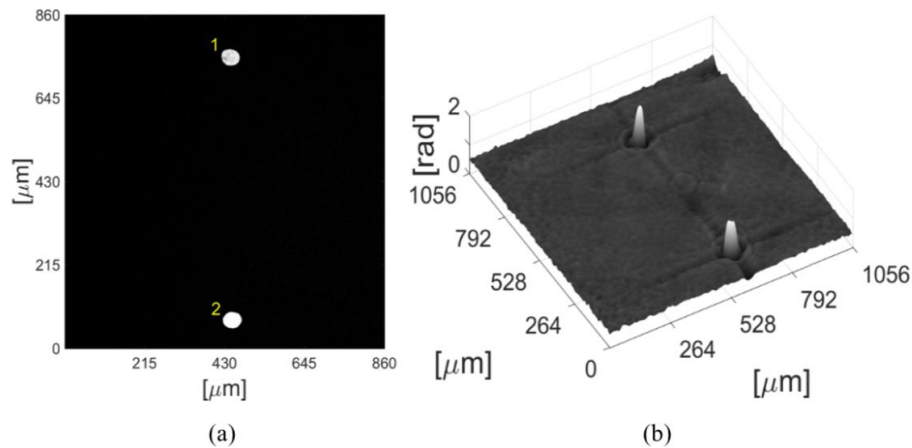
Figure 34. PFA_d (a) confocal and (b) phase magnitude.

There is a direct correlation between the size of the micro-sample and its optical phase magnitude. Nevertheless, if tilt is applied to the PFA when placed in the object arm, the phase magnitude is modified. Thus, three additional tests were performed for PFA_c and PFA_d and the first one, to analyze the impact of this tilt. After processing all the information, phase information does change for each case. However, this variation applies to all the observed particles in the PFAs. Thus, the size classification for each pollen grain remains the same as the one described in Tables 2 and 3.

4.2 Part 2 (Simultaneous inspection DHI+OCT)

The composite was designed to increase its stiffness during the compression test within the elastic deformation. A PMMA matrix of 30 grams is mixed with 5 grams of micro copper particles in a cold mounting process. The resulting polymer is cut in two different sets of prisms: the first set

(M1) has a size of 15x5x4 mm, while in the second one (M2) is 15x5x2 mm to have a different mechanical response (plastic deformation) during the compression tests. For each set, several samples were cut and tested to prove the repeatability and recording speed of the dual inspection set up. The compression range in these tests covers from 10 up to 40 lbf to stay within the elastic range of the samples (see Appendix B). Several images were recorded with both optical techniques, and it is impossible to show all these images in this work, for this reason, was selected individual loads: 12, 16, 20, 24, 28, 32, 36, 40 lbf. As the repeatability of the compression was proved, the following results are the average response for each set M1 and M2.

Figure 35. Average DHI wrapped phase maps for (a) M1 and (b) M2.

Figure 36. Average FD-OCT wrapped phase maps for (a) M1 and (b) M2.

In Fig. 35 shows the DHI wrapped phase maps for M1 and M2 at these selected loads, while in Fig. 36 presents the FD-OCT wrapped phase maps from these same sets and loads. Consider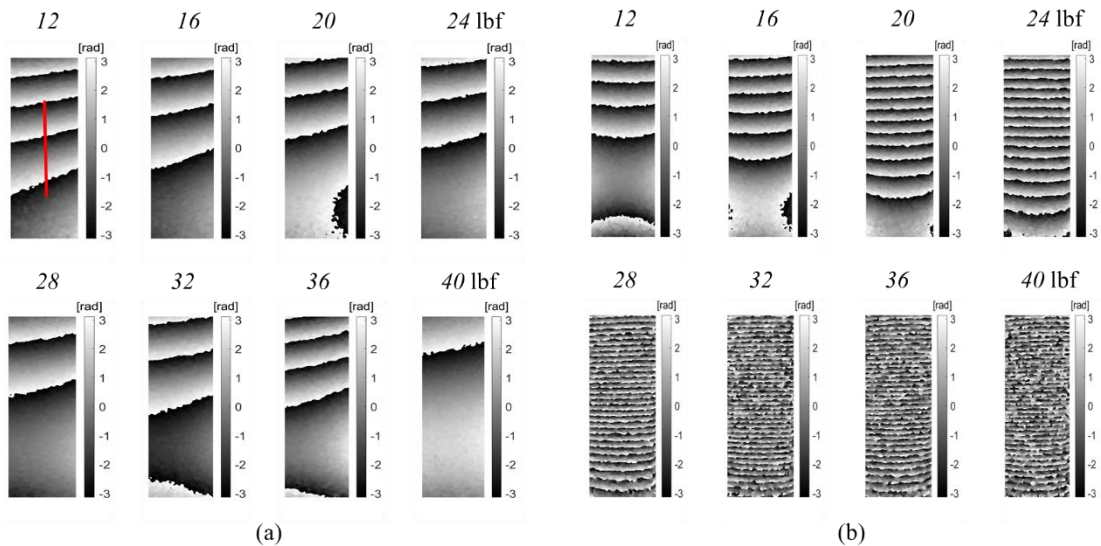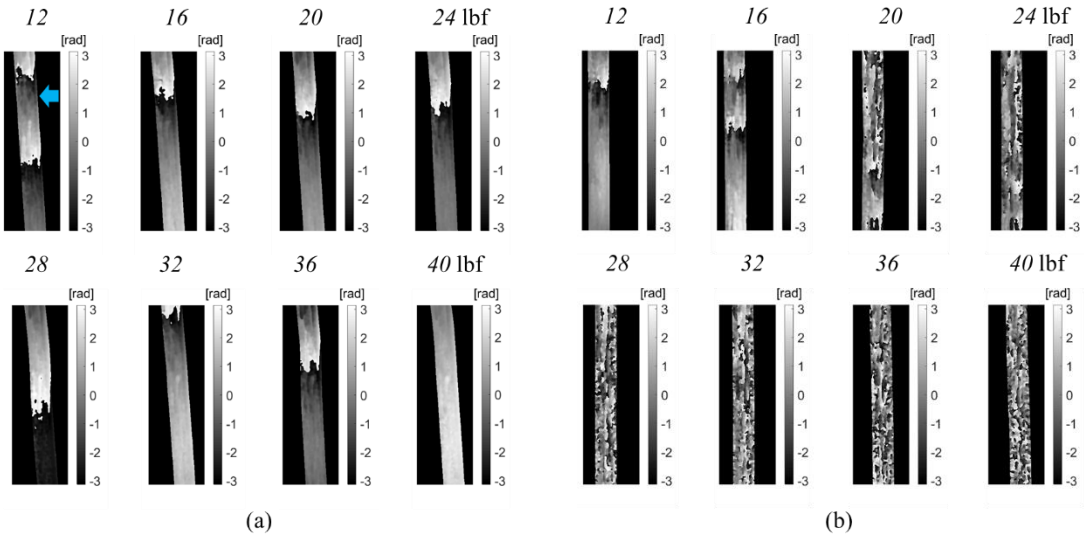ing the axis orientation for these figures (indicated in Fig. 23), the wrapped phase maps from DHI and FD-OCT are in the xy and yz planes, respectively. In Fig. 35(a) is possible to observe the average bending behavior of M1 in the entire range of compression compared with the tilting response of M2 after 24 lbf of compression (see Fig. 35(b)). This bending results from the little opposition of the M2 samples to the compression, which changes the expected bending response to a tilting one (this behavior was expected due to M1 has twice the thickness of M2). However, only with this surface information, it is not possible to determine if M2 leaves the elastic range and moves to the plastic one. By remembering that in the load curve, the elastic range is when the sample is undergone to a maximum load force, and after applying this load, the sample can return to its original shape. Nevertheless, when the load is beyond, the material can suffer a permanent deformation known as the plastic range (observed in Fig. 27(b)). To further analyze this condition, information of the FD-OCT is required. Fig. 36 shows a ~ 1.5mm depth B-scan (along the red line at 12 lbf in Fig. 35(a)), the interface air-composite is indicated with a blue arrow at 12 lbf in Fig. 36(a). Comparing the optical phases of M1 and M2, it is possible to observe that the specimen M1 remains within the elastic range (isotropic). At the same time, M2 starts to be plastic (anisotropic) at 24 lbf, as Fig. 36(b) shows.
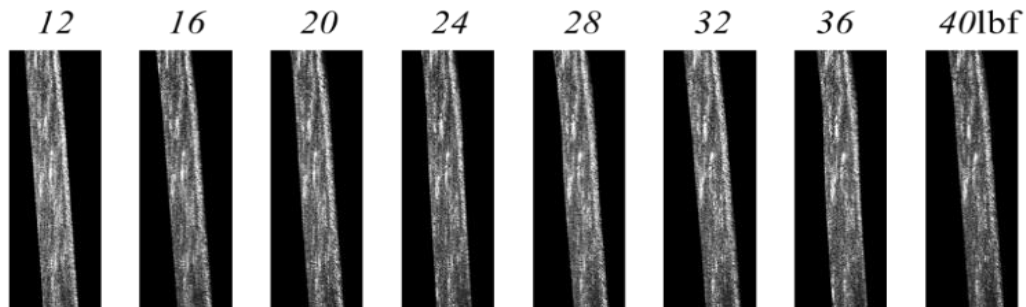
Figure 37. Example of the OCT signal at the selected compression loads for M1.

The OCT signal from the composite specimen's internal scattering points (Fig. 37) helps to analyze the real body motion along the z-axis, a feature not easy to determine with the DHI information. The average compressive deformation for each wrapped phase map is obtained using equation (59). In Fig. 38 and Fig. 39 are presented the displacement maps for DHI and FD-OCT phase maps, respectively. For a quick reference, M1 (blue to red) and M2 (dark red to white) displacement's color scales are different. During the compression test, the surface maximum averaged displacement

reached for M1 and M2 were 1.4 and 9 µm respectively. This behavior should also be replicated with the internal deformation, but once the plastic range is observed (24 lbf), the phase information appears de-correlated. However, this is not followed in the surface (DHI), where a smooth optical phase is registered. Please observe that the maximum deformation is located at the bottom side of the specimen. A notorious movement from left to right is observed in the FD-OCT displacements, especially in M2 (Fig. 39(b)).
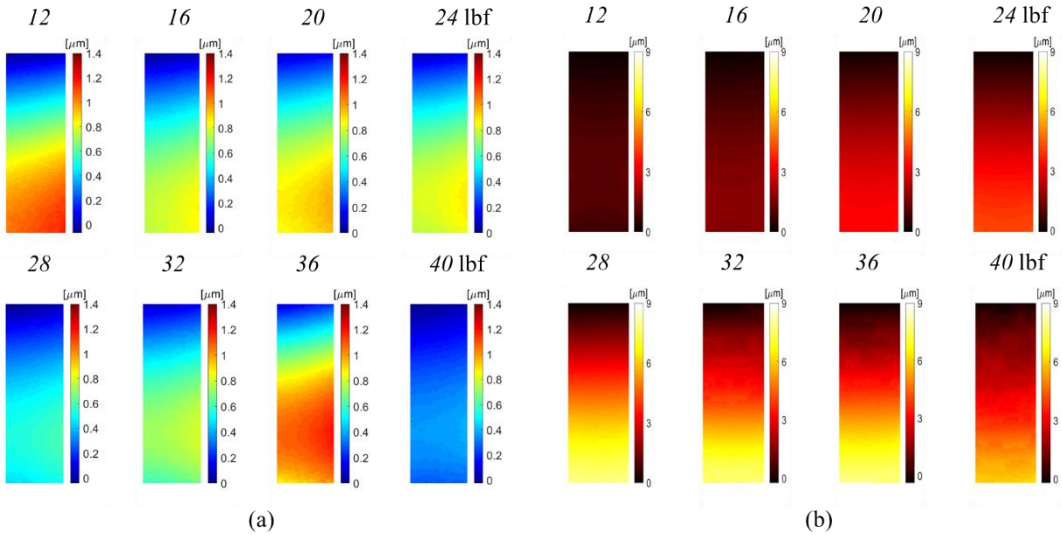
Figure 38. Average DHI displacement maps for (a) M1 and (b) M2.
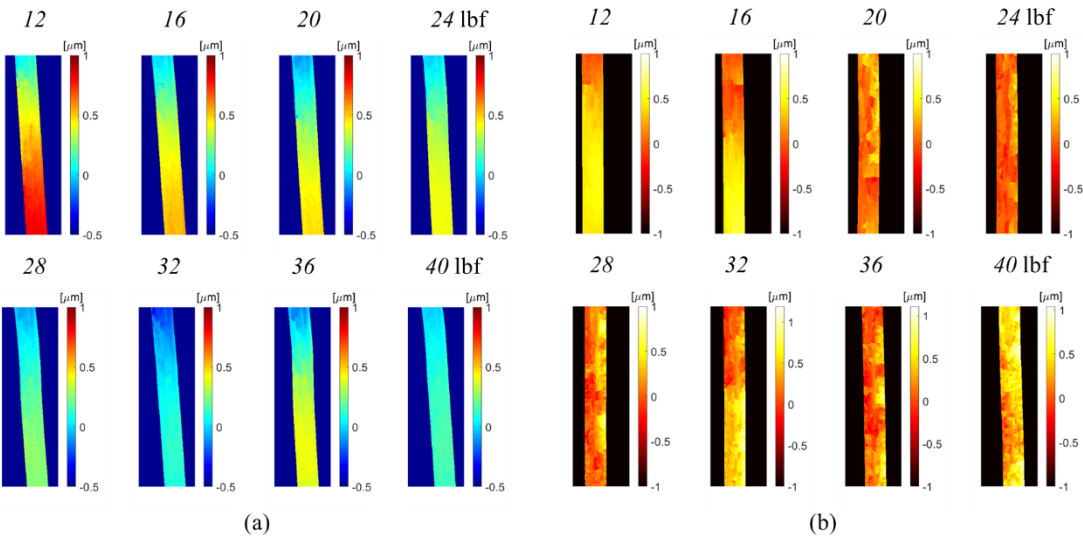
Figure 39. Average FD-OCT displacement maps for (a) M1 and (b) M2.

This movement happens due to the applied compression and the specimen's response while bending or tilting (real body motion). The phase sensitivity is different in both techniques; this allows different displacement magnitudes between DHI and FD-OCT data. The latter helps identify the compressive strength of a mechanical stiffness sample as M1 compared with M2.

DHI gives the surface deformation related to the sample's stiffness while FD-OCT offers information about the internal deformation, which identifies the transition between the isotropic and anisotropic state of the sample.

5. Conclusions and future work

The t-DHI system is a novel optical configuration with a controlled magnification and could inspect semi-transparent biological samples. The system can obtain a phase magnitude related to the dimensions of the sample under study. A calibration pattern is used to validate this optical system. Then, the measurements of the t-DHI system of each PFA sample are compared with their confocal images. Moreover, it is essential to mention that this is the first time that this modified version is used to measure semi-transparent biological samples, driving to a new spectrum of possible applications that may include the study of inorganic samples. This optical configuration was first used to study thermal distributions in liquids [28].

On the other hand, the second optical configuration utilizes, for the first time, a simultaneous inspection with an FD-OCT and DHI systems to track the compression displacements in composite specimens. The advantage is that the sample can be easily prepared. Also, both techniques are non-invasive, and a high resolution from both can be obtained; the latter permits micrometric detection over an internal layer and the surface of the sample. This mechanical information could be used in the material's engineering area to better understand the mechanical behavior of the sample studied within the elastic or plastic range to analyze different mechanical parameters.

To obtain the mechanical behavior of materials during some tests (deformation, tensile strength, compression, fracture, or displacements), some non-invasive optical techniques, such as OCT and DHI, have been employed separately. This work is the first time the DHI and OCT systems have been used simultaneously to inspect the mechanical behavior of composite material when this is undergone to a compressive force. Besides, it is possible to obtain the displacement value for each optical technique. With this information, every sample has a different value displacement due to its dimensions, i.e., two samples were tested, M1 and M2. M1 is twice as thick as M2; for this reason, M2 does not have the same strength as M1 (Fig. 39). This proposed configuration is a new way to measure internal and external information simultaneously in a low scattering material.

Both optical configurations are proof of principle in state of the art, which allows continuing to develop and improve research in transmission digital holographic interferometry for complex samples and deformations. t-DHI could be used in the biomedical area, e.g., to study living cells or analyze the blood dynamics in a full field of view different from the existing methods. The latter is possible due to the possibility of inspecting the sample's surroundings with the same resolution.

The simultaneous (multi-purpose) non-invasive inspection was used to analyze a composite material in a controlled condition. However, the possibilities for a wide application field is just starting. More complex and multi-tasks techniques are considered for new setups. Some target

applications are within the biomedical area to study complex tissues like bones, tendons, teeth, skin, etc. As more techniques are embedded in this configuration, the measuring ranges and resolution are drastically improved to have a full mechanical characterization by optical methods.

6. References

[1] Boudoux, Caroline, "Fundamentals of Biomedical Optics," Pollux Editions, Montréal (2016).

[2] Kaufmann, Guillermo. H. "Advances in Speckle Metrology and Related Techniques," Wiley VCH Verlag GmbH & Co. KGaA, Weinheim. Germany (2011).

[3] Gasvik, Kjell. "Optical Metrology," John Wiley & Sons, Third Edition (2002)

[4] P. Hariharan, B. F. Oreb, and T. Eiju. "Digital phase-shifting interferometry: a simple error-compensating phase calculation algorithm," Applied Optics, **26** (13). 1987.

[5] Bhaduri Basanta, N. Krishna Mohan, M. P. Kothiyal and R.S. Sirohi "Use of spatial phase shifting technique in digital speckle pattern interferometry (DSPI) and digital shearography (DS)," Optics Express, **14** (24), 2006

[6] Yongzhao Du, Guoying Feng, Hongru Li, J. Vargas and Shouhuan Zhou. "Spatial carrier phase-shifting algorithm based on principal component analysis method," Optics Express, **20** (15). 2012.

[7] Takeda, M., Ina, H. and Kobayashi, S., "Fourier-transform method of fringe-pattern analysis for computer-based topography and interferometry," J. Opt. Soc. Am. **72** (1), 156-160, (1982).

[8] Y. Garini, B. J. Vermolen and I. T.Young, "From micro to nano: recent advances in high-resolution microscopy," Curr. Opin. Biotechnol. **16** (1), 3-12 (2005).

[9] A. Lewis, H. Taha, A. Strinkovski, A. Manevitch, A. Khatchatouriants, R. Dekhter and E. Ammann, "Nearfield optics: from subwavelength illumination to nanometric shadowing," Nat. Biotech. **21**, 1378-1386 (2003).

[10] F. Charriere, A. Marian, F. Montfort, J. Kuehn, T. Colomb, E. Cuche, P. Marquet and C. Depeursinge, "Cell refractive index tomography by digital holographic microscopy," Opt. Lett. **31** (2) (2006).

[11] W. Osten, A. Faridian, P. Gao, K. Korner, D. Naik, G. Pedrini, A. Kumar-Singh, M. Takeda, and M. Wilke, "Recent advances in digital holography," App. Opt. **53** (27), G44-G63 (2014).

[12] P. Picart, "New Techniques in Digital Holography," Wiley, (2015).

[13] L. Yu, S. Mohantly, J. Zhang, S. Genc, M. K. Kim, M. Berns and Z. Chen, "Digital holographic microscopy for quantitative cell dynamic evaluation during laser microsurgery," Opt. Express. **17** (14), 12031-12038 (2009).

[14] J. M. Flores-Moreno, F. Mendoza S. and J.C. Estrada, "Holographic otoscope using dual-shot-acquisition for the study of eardrum biomechanical displacements," App. Opt. **52** (8), 1731- 1742 (2013).

[15] M. S. Hernandez-Montes, S. Muñoz, M. De la Torre, J. M. Flores, C. Perez and F. Mendoza-Santoyo, "Quantification of the vocal fold's dynamic displacement," J. Phys. D: Appl. Phys. **49**, 175401 (2016).

[16] C. G. Tavera, M. De la Torre, J. M. Flores-Moreno, M. S. Hernandez-Montes, F. Mendoza-Santoyo, M. Briones and J. Sanchez-Preciado, "Surface structural damage study in cortical bone due to medical drilling," App. Opt. **56** (13), F179 – F188 (2017).

[17] T. Kreis, "Handbook of Holographic Interferometry: Optical and Digital Methods," Wiley, (2004).

[18] Z. Wang, L. Millet, M. Mir, H. Ding, S. Unarunotai, J. Rogers, M. Gillette and G. Popescu, "Spatial light interference microscopy (SLIM)," Opt. Express **19** (2), 1016 – 1026 (2010).

[19] M. K. Kim, "Principles and techniques of digital holographic microscopy," SPIE Reviews **1**, 1 – 50 (2010).

[20] X. Yu, J. Hong, C. Liu and M. K. Kim, "Review of digital holographic microscopy for three-dimensional profiling and tracking," Opt. Eng. **53** (11), 112306-1:112306-21 (2014).

[21] P. Marquet P, B. Rappaz, P. J. Magistretti, E. Cuche, Y. Emery, T. Colomb and C. Depeursinge, "Digital holographic microscopy: a non-invasive contrast imaging technique allowing quantitative visualization of living cells with subwavelength axial accuracy," Opt. Lett. **30** (5), 468 – 470 (2005).

[22] B. Rappaz, P. Marquet, E. Cuche, Y. Emery, C. Depeursinge and P. J. Magistretti, "Measurement of the integral refractive index and dynamic cell morphometry of living cells with digital holographic microscopy," Opt. Express **13** (23), 9361 – 9373 (2005).

[23] I. Crha, J. Zakova, M. Huser, P. Ventruba, E. Lousova and M. Phanka, "Digital holographic microscopy in human sperm imaging," J. Assist. Reprod. Genet. **28**, 725 – 729 (2011).

[24] B. Kemper and G. Bally, "Digital holographic microscopy for live cell applications and technical inspection," App. Opt. **47** (4), A52 – A61 (2007).

[25] C. J. Mann, L. Yu and M. K. Kim, "Movies of cellular and subcellular motion by digital holographic microscopy," BioMedical Eng. Online **5** (2006).

[26] C. Schockaert "Digital Holography Microscopy Applications: Three Dimensional Object Analysis and Tracking," VDM Verlag Dr. Müller, USA, (2009).

[27] S. Rawat, S. Komatsu, A. Markman, A. Anand and B. Javidi, "Compact and field-portable 3D printed shearing digital holographic microscope for automated cell identification," Appl. Opt. **56** (9), D127-D133 (2017).

[28] De la Torre, M. H., Mendoza-Santoyo, F. and Hernández-Montes M. S., "Transmission out-of-plane interferometer to study thermal distributions in liquids," Optics Letters, **43** (4), 871-874, (2018).

[29] De la Torre-Ibarra, M. H., Ruiz, P. D. and Huntley J. M. "Double-shot depth-resolved displacement field measurement using phase-contrast spectral optical coherence tomography," Optics Express. **14** (21), 9643-9656, (2006).

[30] H. D´Antoni, "Arqueoecología: Sistémica y Caótica," CSIC Press, Madrid, España, (2007).

[31] M. Mar Trigo, "Contribución al studio polínico de especies ornamentals: Acanthaceae y Verbenaceae," Acta Botanica Malacitana **18**, 135-146 (1993).

[32] E. L. Ghisalberti, "Review Lantana cámara L. (Verbenaceae)," Elsevier Science Fitoterapia **71**, 467-486 (2000).

[33] J. F. Morton, "Lantana, or red sage (Lantana camara L., [Verbenaceae]), notorious weed and popular garden flower; some cases of poisoning in Florida," Economic Botany, **48** (3), 259-270 (1994).

[34] W. Brostow and H. E. Hagg Lobland, "Materials: Introduction and Applications," John Wiley & Sons (2016).

[35] M. Kutz, "Mechanical Engineers' Handbook: Materials and Engineering Mechanics," 4th ed. USA: Wiley (2015).

[36] R. Li, H. Xia, Z. Xu, Q. Ni and Y. Fu, "U-DMA measurement and dynamic analysis of ultrasonic wave propagation in particulate composites," Composites Science and Technology **151,** 174-183 (2017).

[37] R. Joselin, D. Sudharsan and R.B. Jeen Robert, "Determination of mechanical properties in AlSiC specimen using non destructive method," Proc. of International Conference on Advanced Nanomaterials & Emerging Engineering Technologies (ICANMEET-2013) IEEE, 658-662 (2013).

[38] T. Matheus, C. Kauffman, A. Braz, C. Mota and A. Gomes, "Fracture Process Characterization of Fiber-Reinforced Dental Composites Evaluated by Optical Coherence Tomography, SEM and Optical Microscopy," Braz Dent J. **21** (5), 420-427 (2010).

[39] M. Sinha, R.K. Tyagi and P.K. Bajpai, "Weight Reduction of Structural Members for Ground Vehicles by the Introduction of FRP Composite and Its Implications," Proc. of the International Conference on Modern Research in Aerospace Engineering. 277-290 (2018).

[40] G. Koronis, A. Silva and M. Fontul, "Green composites: A review of adequate materials for automotive applications," Composites: Part B. **44**, 120-127 (2013).

[41] T. Shi, Z. Li, J. Guo, H. Gong and C. Gu, "Research progress on CNTs/CNFs-modified cement-based composites-A review," Construction and Building Materials. **202**, 290-307 (2019).

[42] J. S. Popovics and K.V.L. Subramaniam, "Review of Ultrasonic Wave Reflection Applied to Early-Age Concrete and Cementitious Materials," J Nondestruct Eval. **34**, 267 (2015).

[43] S. Gholizadeh, Z. Leman and B.T.H.T. Baharudin, "A review of the application of acoustic emission technique in engineering," Structural Engineering and Mechanics. **54** (6), 1075-1095 (2015).

[44] S. Gholizadeh, "A review of non-destructive testing methods of composite materials," Procedia Structural Integrity. **1**, 050-057 (2016).

[45] G. E. Dovgalenko, M. S. Haque, A. V. Kniazkov, Y. I. Onischenko, G. J. Salamo and H. A. Naseem, "Stress measurement of deposited SiO2 films on a silicon wafer using dimensional-stability holographic interferometry test," Proc. SPIE. **3134**, 475-485 (1997).

[46] R. C. Youngquist, S. Carr and D. E. N. Davies, "Optical coherence-domain reflectometry: a new optical evaluation technique," Optics Letters. **12** (3), 158-160 (1987).

[47] E. A. Swanson, J. A. Izatt, M. R. Hee, D. Huang, C. P. Lin, J. S. Schuman, C. A. Puliafito and J. G. Fujimoto, "In vivo retinal imaging by optical coherence tomography," *Optics Letters.* **18** (21), 1864-1866 (1993).

[48] A. F. Fercher, C. K. Hitzenberger, W. Drexler, G. Kamp, H. Sattmann, L. Schmetterer, I. Strasser and C. Unfried, "In-vivo dual-beam optical coherence tomography," Proc. SPIE. **2083**, 356-362 (1994)**.**

[49] M. Bechmann, M. J. Thiel, A. S. Neubauer, S. Ullrich, K. Ludwig, K. R. Kenyon and M. W. Ulbig, "Central Corneal Thickness Measurement with a Retinal Optical Coherence Tomography Device Versus Standard Ultrasonic Pachymetry," Cornea. **20** (1), 50-54 (2001).

[50] J. Welzel, E. Lankenau, R. Birngruber and R. Engelhardt, "Optical coherence tomography of the human skin," J. Am Acad Dermatol. **37** (6), 958-963 (1997).

[51] J. Welze, "Optical coherence tomography in dermatology: a review," Skin Research and Technology. **7**, 1-9 (2001).

[52] J. Walther, C. Schnabel, F. Tetschke, T. Rosenauer, J. Golde, N. Ebert, M. Baumann, C. Hannig and E. Koch, "In vivo imaging in the oral cavity by endoscopic optical coherence tomography," Journal of Biomedical Optics. **23** (7), 071207 (2018).

[53] V. Damodaran, S. R. Rao and N. J. Vasa, "Optical coherence tomography based imaging of dental demineralization and cavity restoration in 840 nm and 1310 nm wavelength regions," Optics and Lasers in Engineering. **83**, 59-65 (2016).

[54] I.-K. Jang, B. E. Bouma, D.–H. Kang, S.-J. Park, S.-W. Park, K.-B. Seung, K.-B. Choi, M. Shishkov, K. Schlendorf, E. Pomerantsev, S. L. Houser, H. T. Aretz and G. J. Tearney, "Visualization of Coronary Atherosclerotic Plaques in Patients Using Optical Coherence Tomography: Comparison With Intravascular Ultrasound," Journal of the American College of Cardiology. **39** (4), 604-609 (2002).

[55] H. G. Bezerra, M. A. Costa, G. Guagliumi, A. M. Rollins, D. I. Simon, "Intracoronary Optical Coherence Tomography: A Comprehensive Review," JACC: Cardiovascular Interventions. **2** (11), 1035-1046 (2009).

[56] P. Targowski, B. Rouba, M. Góra, L. Tymińska-Widmer, J. Marczak and A. Kowalczyk, "Optical coherence tomography in art diagnostics and restoration," Appl. Phys. A. **92**, 1-9 (2008).

[57] P. Antoniuk, M. R. Strąkowski, J. Pluciński and B. B. Kosmowski, "Non-destructive inspection of anti-corrosion protective coating using optical coherent tomography," Metrol. Meas. Syst. **XIX** (2), 365-372 (2012).

[58] A. K. S. Braz, B. B. C. Kyotoku, R. Braz and A. S. L. Gomes, "Evaluation of crack propagation in dental composites by optical coherence tomography," Dental Materials. **25**, 74-79 (2009).

[59] P. Liu, R. M. Groves and R. Benedictus, "3D monitoring of delamination growth in a wind turbine blade composite using optical coherence tomography," NDT&E International. **64**, 52-58 (2014).

[60] D. Stifter, E. Leiss-Holzinger, Z. Major, B. Baumann, M. Pircher, E. Götzinger, C. Hitzenberger and B. Heise, "Dynamic optical studies in materials testing with spectral-domain polarization-sensitive optical coherence tomography," Optics Express. **18** (25), 25712-25725 (2010).

[61] P. Liu, R. Groves and R. Benedictus, "Non-destructive evaluation of delamination growth in glass fiber composites using optical coherence tomography," Proc. SPIE. **9063**, 90631M-1-90631M-9 (2014).

[62] R. Yamada, H. Okura, T. Kume, K. Fukuhara, T. Koyama, T. Higa, Y. Neishi, K. Yoshida and S. Uemura, "Impact of stent platform on longitudinal stent deformation: an in vivo frequency domain optical coherence tomography study," Cardiovas Interv and Ther. **32**, 199-205 (2017).

[63] M. Briones-R, M. H. De la Torre-I, J. M. Flores-M, C. G. Tavera, J. M. Luna and F. Mendoza, "3D homogeneity study in PMMA layers using Fourier domain OCT system," Optics and Lasers in Engineering. **86,** 181-196 (2016).

[64] M. H. De la Torre-Ibarra, P. D. Ruiz and J. M. Huntley, "Double-shot depth-resolved displacement field measurement using phase-contrast spectral optical coherence tomography," Optics Express. **14** (21), 9643-9656 (2006).

[65] D. V. Nelson, "Residual Stress Determination by Hole Drilling Combined with Optical Methods," Experimental Mechanics. **50,** 145-158 (2010).

[66] V. Martinez-Garcia, M. Wenzelburger, A. Killinger, G. Pedrini, R. Gadow and W. Osten, "Residual Stress Measurement with Laser-Optical and Mechanical Methods," Advanced Materials Research. **996**, 256-261 (2014).

[67] S. Li, K. D. Mohan, W. W. Sanders and A. L. Oldenburg, "Toward soft-tissue elastography using digital holography to monitor surface acoustic waves," Journal of Biomedical Optics. **16** (11), 116005 (2011).

[68] M. H. De la Torre and F. Mendoza Santoyo, "Interferometric study on birds' feathers," Journal of Biomedical optics. **18** (5), 056011 (2013).

[69] Y. Yamaguchi, K. Horiguchi, Y. Shindo, D. Sekiya and S. Kumagai, "Fracture and deformation properties of Ni-Fe superalloy in cryogenic high magnetic field environments," *Cryogenics*. **43**, 469-475 (2003).

[70] B. D. Beake, G. S. Fox-Rabinovich, S. C. Veldhuis and S. R. Goodes, "Coating optimisation for high speed machining with advanced nanomechanical test methods," Surface & Coating Technology. **203**, 1919-1925 (2009).

[71] P. N. Eleni, I. Katsavou, M. K. Krokida, G. L. Polyzois and L. Gettleman, "Mechanical behavior of facial prosthetic elastomers after outdoor weathering," Dental Materials. **25**, 1493-1502 (2009).

[72] A. Qudoos, H. G. Kim, A-U. Rehman and J.-S. Ryou, "Effect of mechanical processing on the pozzolanic efficiency and the microstructure development of wheat straw ash blended cement composites," Construction and Building Materials. **193**, 481-490 (2018).

[73] S. Manteghi, A. Sarwar, Z. Fawaz, R. Zdero and H. Bougherara, "Mechanical characterization of the static and fatigue compressive properties of a new glass/flax/epoxy composite material using digital image correlation, thermographic stress analysis, and conventional mechanical testing," Materials Science & Engineering C. **99**, 940-950 (2019).

[74] P. Guillemin, "Fuzzy logic applied to motor control," IEEE Transactions on Industry Applications. **32** (1), 51-56 (1996).

[75] J. N. Rai, M. Singhal and M. Nandwani, "Speed control of DC motor using fuzzy logic technique," IOSR Journal of Electrical and Electronics Engineering. **3** (6), 41-48 (2012).

[76] I. H. Usoro, U. T. Itaketo and M. A. Umoren, "Control of a DC motor using fuzzy logic control algorithm," Nigerian Journal of Technology. **36** (2), 594-602 (2017).

[77] C. G. Tavera Ruiz, M. H. De La Torre-Ibarra, J. M. Flores-Moreno, C. Frausto-Reyes, and F. Mendoza Santoyo, "Cortical bone quality affectations and their strength impact analysis using holographic interferometry," Biomedical Optics Express. **9**, 4818-4833 (2018).

Appendix A. Biological samples

As was mentioned in section 3.1.3, the samples used are pollen grains from the Lantana flower. It is well known that the pollen is a kind of powder (sum of several pollen grains) produced within the flower's anthers. The male reproductive cell, formed by several layers of the flower, is found within each pollen grain. The intine is the internal layer, while the exine is the outer one, the latter being resistant to critical conditions [30]. The Lantana plant grows mainly in American regions with tropical and warm climates, so it is possible to find several species [31, 32]. It is an easy to adapt plant, which hence is considered as invasive to local environments such as different places of Mexico and the United States of America [33].

In Fig. 40 shows a Lantana flower used to extract the pollen grains for the tests.

Figure 40. Local Lantana flower is used to extract the pollen grain samples.

The pollen grains collected use a set of microscope glass-slides as the first containers. Care has to be taken to avoid electrostatic conditions during the collection process to prevent clusters of pollen grains. An optical microscope (Leica DM3000 LED) was used to observe and evenly distribute several independent pollen grains on the microscope slides. Once the pollen particles were isolated, a fixation process was used. As the interferometer works in transmission, several fixation mediums were tested, but many of them distorted the object beam or introduce diffraction patterns, as seen on the NPS.

After several tests, the HistoChoice® mounting solution (Amresco) was selected. However, to avoid a wavefront distortion when the solution solidifies, a second slide is placed over the first one, leaving the fixation solution with the pollen grains between them. This arrangement will be referred to as the pollen fixation arrangement (PFA), see Fig. 23.

Appendix B. Synchronization and method of calibration

B.1 Compression control

Fig. 41 shows a general schematic view of the mechatronic system, which performs the repeatable and controlled compression test. The CTM's structure comprises a bottom plate (BP) where the sample is situated during the test, a top plate (TP), which has vertical displacement and compresses the composite specimen. A DC motor can apply a torque up to 3 kg-cm using gears and screws that convert this torque into a compression force limited to 300 lbf (vertical motion of the TP) in the CTM. A load cell attached to the bottom plate transforms the applied load on the sample into a voltage conditioned (in the signal conditioning stage) to then be sent to the MSP430 development board. Then it is converted by an analog to digital (A/D) conversion module (inside the microcontroller MSP430 µC) into digital values. These digital values are sent to a PC via USB (through the UART module of the MSP430 µC and a USB/UART conversion stage of the MSP430 development board). The PC reads those values and translates them into force, which is used to determine the DC motor operation. A power module driver powers the motor with a square wave controlled by a pulse width modulation (PWM) generator of the MSP430 µC. Once the PC processes the force value, it sends a new value of the PWM duty cycle to the µC.
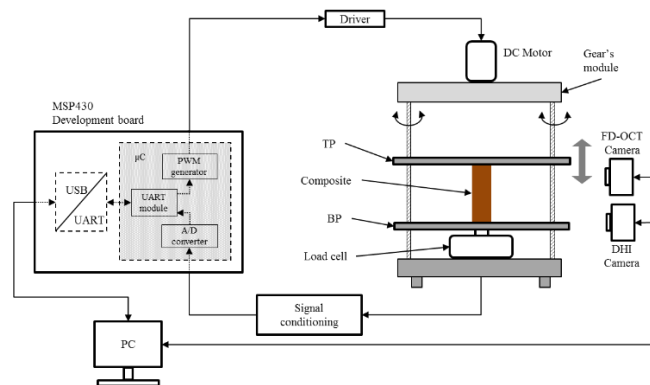

Figure 41. Schematic view of the mechatronic system.

A specimen colocation routine is followed every time that a sample is tested. In this routine, besides the placement of the sample, a load of 0.8 lbf is applied to avoid rigid body motion, and then the preloading process starts. Here, the composite is compressed up to a user-defined preload value, which is the initial force value of the further loading process. The preload process cycle compresses the sample using the same PWM duty cycle, registering all the force values. With the preload values stored in the load vector, a slope trend estimation is carried out, analyzing the last five load values. It

is assumed that at the end of the preload process, the "n" index indicates the final preload value. Two slopes are calculated: the first one (m1) is obtained with the n and n-3 points, while the second one (m2) results with the n-1 and n-4 as Fig. 42 shows. An average slope is obtained using m1 and m2, and it is considered the reference slope (m_{ref}) to be kept during the entire compression test. A valid deviation range around m_{ref} is defined as $m_{ref} - range \leq m_{est} \leq m_{ref} + range$. Here, m_{est} is the currently estimated slope during the compression test, and range is determined as m1 – m2 (once the sloping trend is defined, the load routine starts).
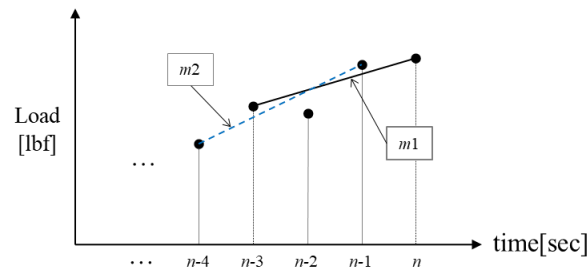

Figure 42. Slope trend analysis considering the last five load values of the preload.

Fig. 43 shows the flow chart of the loading process, where the user sets the maximum load value to be reached by the CTM. Then, the load process cycle begins calculating the slope trend estimation (m_{est}) continuously, and according to this and based on fuzzy logic criteria, a δ factor value is adjusted to modify the PWM duty cycle. Afterward, a new duty cycle value is calculated by adding the δ factor and sent every time to the DC motor.
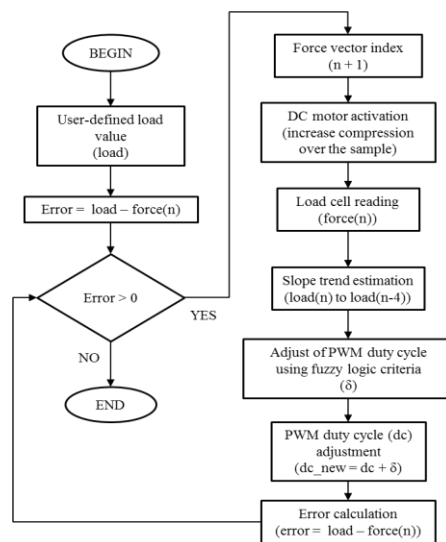

Figure 43. Flow chart of the loading procedure.

The slope trend estimations are performed after each load reading to keep constant the load-time curve during the test. The slope of this curve is related to the CTM compression force and the PWM duty cycle applied to the DC motor using the δ factor [74-76]. The fuzzy sets used to relate m_{est} with δ are shown in Fig.44. It is possible to see that $m_{est} = m_{ref}$ when δ = 0 (meaning that the duty cycle is not modified). However, as m_{est} gets close to $m_{ref} + range$ the δ factor tends to be -1, reducing the duty cycle and the compression load applied by the DC motor. An opposite situation happens when m_{est} is closer to $m_{ref} - range$, and the duty cycle is incremented. Even when m_{est} is below $m_{ref} - range$ or above $m_{ref} + range$, the δ factor takes a higher value to keep the load–time curve within the specific slope range.
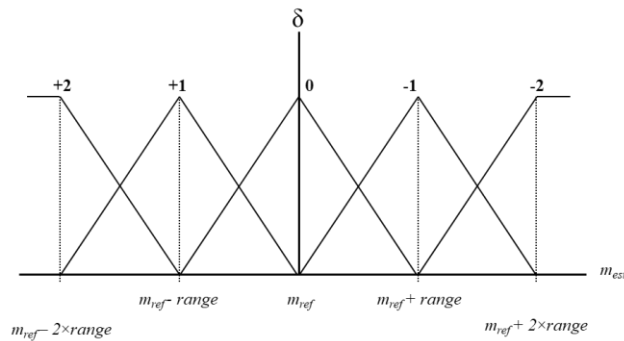

Figure 44. Fuzzy sets are used to assign the δ factor.

B.2 Continuous load test

Before the characterization of the composite and once the CTM repeatability was tested [77], a compression test is performed to analyze the load application ratio and the cameras' synchronization. The CTM applies a continuous stepped compression to a sample while both cameras recorded several images per load step. The latter generates a series of interference images that make it possible to observe the sample's external and internal deformation in the entire range of the compression test. Please note that both optical systems are two state-based techniques, which means that two different images are required to retrieve a phase map. These images represent the reference (*l- Δl*) and the interest (*l*) load. To determine this, a *Δl* was proposed to have a uniform distribution among the readings. For this purpose, several tests were performed to find a *Δl* that works with both interferometric signals. After those tests, the value of *Δl* was set at -0.5 lbf. E.g. to obtain the information at 15 lbf, a second image at 14.5 lbf is used.